Variational and 2D Finite Element Formulations for Size-dependent Elasticity and Piezoelectricity

by

Bradley T. Darrall

A thesis submitted to the Faculty of the Graduate School of
The State University at Buffalo in partial fulfillment of the
requirements for the degree of

Master of Science

Department of Mechanical and Aerospace Engineering
University at Buffalo State University of New York
Buffalo, New York 14260 USA

June 2015

ACKNOWLEDGEMENTS

This thesis is the culmination of years of interesting, thought provoking, and enjoyable research under my advisor and mentor, Dr. Gary Dargush. I would like to thank him for his guidance over the last half decade, not only in the realm of science and engineering, but in all facets of life. His ability to breakdown complicated concepts and make them easy to understand is second to no one I have met. I surely would not be where I am today without his help.

I would also like to thank a few others that have been part of my research experience at the University at Buffalo, including Alireza Hadjesfandiari, whose work comprises nearly all of the theory that this thesis is based on, and also Arezoo Hajesfandiari, Georgios Apostolakis, and Richard Bottom for countless interesting conversations along the way.

Finally, I would like to acknowledge my parents. Their unconditional love and unwavering support has allowed me to follow my dreams since the day I was born.

TABLE OF CONTENTS

LIST OF FIGURES

LIST OF TABLES

ABSTRACT

Size-dependent elasticity and piezoelectricity variational principles are developed based on recent advances in couple-stress theory and the introduction of an engineering mean curvature vector as energy conjugate to the couple-stresses. It is shown that size-dependent piezoelectricity, sometimes referred to as flexoelectricity, is a straightforward extension of consistent couple-stress elasticity, with electric field and mechanical mean-curvature being thermodynamically coupled. These new variational formulations provide a base for developing couple-stress and size-dependent piezoelectric finite element approaches. By considering the elastic portion of the total potential energy functional to be not only a function of displacement, but of an independent rotation as well, we avoid the necessity to maintain C^1 continuity in the finite element methods (FEM) that we develop here. The result is a mixed formulation, which uses Lagrange multipliers to constrain the rotation field to be compatible with the displacement field. Interestingly, this formulation has the noteworthy advantage that the Lagrange multipliers can be shown to be equal to the skew-symmetric part of the force-stress, which otherwise would be cumbersome to calculate. Creating new consistent couple-stress and size-dependent piezoelectric finite element formulations from these variational principles is then a matter of discretizing the variational statement and using appropriate mixed isoparametric elements to represent the domain of interest. The new formulations are then applied to many illustrative examples to bring out important characteristics predicted by consistent couple-stress and size-dependent piezoelectric theories.

CHAPTER ONE

1 INTRODUCTION

It is well known that classical continuum mechanics cannot predict the behavior of materials for very small length scales. While molecular mechanics theories have certainly enjoyed some success, these approaches are only computationally feasible for collections of particles of quite limited spatial and temporal extent. This is the true motivation for developing a size-dependent continuum theory, such as the fully-consistent linear elastic couple-stress theory that provides the foundation for the work here. Recent advances in couple-stress theory have resolved many of the long-standing problems that previous size-dependent continuum theories have had. In particular, some of the more important discoveries are that of the skew-symmetric nature of the couple-stress tensor and identification of mean curvature tensor as the correct second measure of deformation, as opposed to strain-gradient or other kinematic quantities that have been advocated previously. Furthermore, in this fully-consistent skew-symmetric couple-stress theory, for the isotropic case, there is a single new material property, l, with the dimensions of length. The inclusion of couple-stress effects then becomes important for problems having characteristic geometry or loading on the order of l or smaller.

The idea of a higher order continuum theory that included couple-stress first came from Voigt (1887), but the actual formulation was developed later by the Cosserats (1909) in

the early 20th century. Their original theory considered displacement and rotation to be separate fundamental kinematic quantities. This assumption is perfectly acceptable for approximate beam and plate theories, which represent one and two-dimensional structural elements embedded in a higher three-dimensional space. However, such is not the case for a three-dimensional continuum and a full justification of this independence of displacement and rotation fields remains unresolved to this day.

After receiving little attention for many years the Cosserat theory was revisited, but instead of considering rotation independent of displacement, it was instead constrained to be compatible with the displacement field. These new constrained theories, which are more consistent with classical continuum approaches, became known as couple-stress theories. The original couple-stress theories, which came from Toupin (1962), Mindlin and Tiersten (1962), and Koiter (1964), suffer from indeterminacy of the spherical part of the couple-stress tensor, as well as the inclusion of the body couple in the relation for the force-stress tensor. Consequently, these theories have been in the past referred to as inconsistent or indeterminate couple-stress theories.

Subsequent theories along these lines involving couple-stress are referred to as second gradient and strain-gradient theories, which mainly differ in the measures of deformation that are considered. The measures of deformation consist of various combinations of strain, curvature and strain-gradient. In these theories, the gradient of the rotation vector is typically considered to be the curvature tensor. The true underlying issue with these

theories, however, is that the proposed measures of deformation are not the correct energy conjugate pair of the couple-stress tensor.

Soon after the development of the original couple-stress theories people began to develop another branch of higher order theories that more closely resembled the Cosserat theory. The idea of microrotation, a field independent of displacement, was again considered to be a fundamental kinematic quantity in an attempt to remedy the aforementioned issues with inconsistent couple-stress theories. Mindlin (1965, 1968), Eringen (1968) and Nowacki (1986) were the first to revive these Cosserat theories that now are more commonly referred to as micropolar theories. Although these theories have been applied broadly, the inclusion of microrotation as a kinematic quantity is extraneous and does not represent a true continuum mechanics concept. If the original couple stress theories (Toupin, 1962; Mindlin 1962; Koiter, 1964) had not encountered the obstacles mentioned above, then perhaps there would have been no need to revert to the Cosserat ideas, which stem from the consideration of lower-dimensional structural elements (e.g., beams, plates, shells) embedded in three-dimensional space. In these cases, independent rotational degrees of freedom are perfectly justified. The difficulty for micropolar theories comes in attempting to embed a full three-dimensional continuum with independent rotations into three-dimensional space.

Recently a new couple-stress theory has been developed that resolves all issues that prior couple-stress theories have had. This new fully-determinate, consistent couple-stress

theory (Hadjesfandiari and Dargush, 2011) uses virtual work and admissible boundary condition considerations to reveal the skew-symmetric nature of the couple-stress tensor and shows that mean curvature is in fact the correct energy conjugate measure of deformation. The variational formulations presented in the current thesis will be based upon this new consistent theory. Although this consistent couple stress theory uses some elements from Mindlin and Tiersten (1962) and Koiter (1964), it cannot be taken as a special case; in fact, for isotropic materials, the new consistent theory is explicitly excluded based upon their definitions of the permissible material parameter ranges. Rather, these indeterminate theories can be considered as an initial inconsistent version of this final couple stress theory. Mindlin and Tiersten (1962) and Koiter (1964) used the gradient of the rotation as the curvature tensor. Unfortunately, this is not the proper measure of deformation energetically conjugate to couple stresses, which then creates indeterminacy in the spherical part of the couple-stress tensor, as mentioned above. For more explanation, see Hadjesfnadiari and Dargush (2013), especially Appendix A. Hadjesfandiari (2013) also derives the skew-symmetric character of the couple stresses purely from tensorial arguments.

The number of analytical solutions available for couple-stress and micropolar theories within the context of elasticity is very limited and therefore numerical methods must be explored. Within the field of solids and structures, the finite element method (FEM) is the most widely used numerical method and accordingly many couple-stress and micropolar FEM formulations have been developed, including those by Hermann (1983), Wood(1988), Providas and Kattis (2002), Padovan (1978), Shu et al. (1999) and

Amanatidou and Aravas (2001). All of these are mixed formulations that include additional degrees of freedom for rotation to simplify the problem, such that only C^0 continuity is required. The previous formulations mainly differ in which specific theory they are based upon, all of which have various flaws that were mentioned previously, as well as how the rotational degrees of freedom are constrained. Chapter 2 provides all of the detail for consistent couple stress elasticity, along with the corresponding variational statements, weak forms, finite element methods and illustrative two-dimensional applications.

Over the last half-century, piezoelectric phenomena have had a profound impact on the development of many technologies. More recently, however, there is a push to develop technology on increasingly minute length scales, where it has been discovered that classical piezoelectric theory is not sufficient for describing all of the observed linear electromechanical coupling behavior. For modeling of small-scale electromechanical phenomena, a size-dependent piezoelectric theory, in some forms known as flexoelectricity, is necessary. These proposed theories are higher order continuum theories that include coupling between a higher order measure of deformation, such as strain-gradient or curvature, and the electric polarization field. Interestingly, it is shown both experimentally and theoretically that these size-dependent piezoelectric effects can occur in classically non-piezoelectric materials and, in particular, centrosymmetric cubic and isotropic materials.

Classical piezoelectricity describes the linear electromechanical coupling between strain or stress and the polarization within an anisotropic dielectric body. The groundbreaking experimental work of the Curie brothers established the foundation for piezoelectricity (Curie and Curie, 1880), which was subsequently placed on a firm theoretical base by Voigt (1910). The well-known monograph by Cady (1964) provides a comprehensive review of developments through the middle of the twentieth century. Since then countless technologies have taken advantage of piezoelectric phenomenon, from high-tech instrumentation to everyday commercial products.

The idea of size-dependent piezoelectric effects was first discussed in Kogan (1964), Meyer (1969) and Tagantsev (1986) and was eventually coined "flexoelectric" effects. More recently size-dependent piezoelectric effects and electromechanical coupling effects in centrosymmetric bodies have been studied by numerous researchers (e.g., Mishima et al., 1997; Shvartsman et al., 2002; Buhlmann et al., 2002; Cross, 2006; Maranganti et al., 2006; Harden et al., 2006; Zhu et al., 2006; Sharma et al., 2007; Majdoub et al., 2008; Maranganti and Sharma, 2009; Resta, 2010; Baskaran et al., 2011; Catalan et al., 2011). With the increasing development of micro- and nano-scale technology, there is a need to model this size-dependent piezoelectric behavior, which can have useful effects for small characteristic geometries and cannot be captured using classical piezoelectric theory. This size-dependent behavior can be incorporated by considering that besides strain, the polarization in a dielectric body may be coupled to higher order measures of deformation as well. It is logical when formulating a size-dependent piezoelectric theory to consider a size-dependent elasticity theory and then

introduce electromechanical coupling via thermodynamic considerations. Wang et al. (2004) consider the gradient of rotation as the higher order measure of deformation, which then is coupled to the polarization. Others have considered strain gradients and various forms of curvature to be coupled to the electric polarization (Tagantsev, 1986; Sharma et al., 2007; Eliseev et al. (2009). The previous theories suffer either from various incompatibility with the underlying Maxwell equations of electromagnetics (Hadjesfandiari, 2014) or with inherent indeterminacies due to the dependence on original couple-stress elasticity theories, as first developed by Toupin (1962), Mindlin and Tiersten (1962) and Koiter (1964).

As noted above, the consistent couple-stress theory that has been developed recently remedies all of the issues that prior size-dependent elasticity theories had (Hadjesfandiari and Dargush, 2011, 2013). In this new theory, the mean curvature tensor is shown to be the correct higher order measure of deformation, while the skew-symmetric nature of the couple-stress tensor is revealed, making the theory fully determinate. More recently, in Hadjesfandiari (2013), a new consistent size-dependent piezoelectric theory is advanced by using the discoveries regarding size-dependent elasticity. This new theory has coupling between the skew-symmetric mean curvature tensor and the polarization field, which allows for piezoelectric behavior even in centrosymmetric materials. Couple-stress effects are also inherently present in this theory (Hadjesfandiari, 2013).

In order for technology to take full advantage of piezoelectric phenomena, numerical methods for accurate modeling must be developed. Similar to most continuum theories, the only available analytical solutions for piezoelectric problems are based on very simple geometry and boundary conditions. To date, many finite element based formulations have been developed for modeling classical piezoelectricity. Benjeddou (2000) gives an excellent review of the advances in finite element approaches to modeling piezoelectric structural elements. Other notable works on finite element formulations for classical piezoelectricity include those of Allik and Hughes (1970) for applications to vibration, Hwang et al. (1993) for modeling of sensors and actuators, and Gaudenzi and Bathe (1995) for general continua analysis.

Despite the many efforts to advance numerical methods used to model and simulate classical piezoelectricity, very little work has been done in developing numerical methods to model size-dependent piezoelectric effects. Consequently, in this thesis, a mixed finite element (FE) formulation is developed that can be applied to solve planar size-dependent piezoelectric problems. Because much work has already been done to develop finite element formulations for classical piezoelectric effects that can only exist in non-centrosymmetric anisotropic materials, we instead restrict ourselves to centrosymmetric materials. Most interestingly, higher order size-dependent piezoelectric effects can still be present for such materials, which in turn suggest many potential new applications at the micro- and nano-scale.

The formulation presented in this thesis is based on the consistent size-dependent piezoelectric theory of Hadjesfandiari (2013), while the corresponding finite element formulation can be considered an extension of the consistent couple-stress variational finite element approach developed in chapter 2 of the present work. This new size-dependent piezoelectric FE formulation is based on the variational problem that is derived from considering the stationarity of a total electromechanical enthalpy functional. The electric field is coupled to the mean curvature within the electromechanical enthalpy, which allows for size-dependent piezoelectric effects. By considering the rotation to be an additional field variable and then enforcing rotation-displacement compatibility via Lagrange multipliers, the coupled size-dependent piezoelectricity problem is reduced to a C^0 variational problem. Again these Lagrange multipliers conveniently are equal to the skew-symmetric portion of the stress tensor. Details of the governing equations, variational methods and finite element formulations are provided in chapter 3.

Throughout this work, standard tensor index notation will be used where subscripts i, j, k, and l will range from 1 to 3 representing Cartesian coordinates x, y, and z. Repeating of indices implies summing over all values for that index. Additionally, ε_{ijk} is the Levi-Civita alternating symbol and δ_{ij} is the Kronecker delta. When formulating finite element methods, vector notation is used for convenience, where bold face characters will be used to represent vectors and matrices.

CHAPTER TWO

2 COUPLE STRESS SIZE-DEPENDENT ELASTICITY

2.1 Overview of Linear Couple Stress Theory

In this section, a brief overview is provided of the important concepts and relations in the recent consistent couple-stress theory for solids. The focus is primarily on the relations that are pertinent to the development of the couple-stress finite element formulation presented here. For a more detailed discussion on the theory, the reader is referred to Hadjesfandiari and Dargush (2011).

From couple-stress theory, a general three dimensional body under quasistatic conditions is governed throughout its volume V by the following equilibrium equations coming from linear and angular momentum balance, respectively,

$$\sigma_{ji,j} + \bar{F}_i = 0 \tag{1}$$

$$\mu_{ji,j} + \varepsilon_{ijk}\sigma_{jk} = 0 \tag{2}$$

where σ_{ji} and μ_{ji} are the force-stresses and couple-stresses, respectively, while $\bar{F}_i$ represents applied body forces. The consideration of body couples is shown to be redundant in Hadjesfandiari and Dargush (2011). All body couple systems can be replaced by an equivalent system of body forces and surface tractions.

In addition, the body is subject to boundary conditions on the surface S. Let us assume that the natural boundary conditions take the form

$$t_i = \bar{t}_i \quad \text{on} \quad S_t \tag{3a}$$

$$m_i = \bar{m}_i \quad \text{on} \quad S_m \tag{3b}$$

while the essential boundary conditions can be written

$$u_i = \bar{u}_i \quad \text{on} \quad S_u \tag{4a}$$

$$\omega_i = \bar{\omega}_i \quad \text{on} \quad S_\omega \tag{4b}$$

Here t_i and m_i represent the force-tractions and moment-tractions, respectively, while u_i and ω_i are the displacements and rotations, respectively, and the overbars denote the specified values. For a well-defined boundary value problem, we should have $S_t \cup S_u = S$, $S_t \cap S_u = \emptyset$ and $S_m \cup S_\omega = S$, $S_m \cap S_\omega = \emptyset$.

From the theoretical development in Hadjesfandiari and Dargush (2011), the normal component of $\bar{m}_i$ is zero and the normal component of $\bar{\omega}_i$ cannot be specified. In general, the moment traction m_i has only a bending effect on the boundary surface, whether or not this quantity is specified.

In general, the relations between force-stress and force-traction, and couple-stress and moment-traction can be written

$$t_i = \sigma_{ji} n_j \tag{5a}$$

$$m_i = \mu_{ji} n_j \tag{5b}$$

where n_i represents the outward unit normal vector to the surface S.

Regarding the kinematics, we may take the gradient of the displacement field and split it into its symmetric and skew-symmetric parts, such that

$$u_{(i,j)} = e_{ij} = \frac{1}{2}(u_{i,j} + u_{j,i}) \tag{6a}$$

$$u_{[i,j]} = \omega_{ij} = \frac{1}{2}(u_{i,j} - u_{j,i}) \tag{6b}$$

where the parenthesis around the indices represent the symmetric part of the tensor, while the square brackets indicate the skew-symmetric part of the tensor. Here we recognize e_{ij} as the linear strain tensor and ω_{ij} as the rotation tensor, under infinitesimal deformation theory. Because ω_{ij} is a skew-symmetric tensor with three independent values, it can be represented by an axial or pseudo-vector. According to the right hand convention, the rotation vector dual to ω_{ij} should be defined as follows:

$$\omega_i = \frac{1}{2}\varepsilon_{ijk}\omega_{kj} \tag{7a}$$

Then, the relationship between displacement and rotation can be expressed as

$$\omega_k = \frac{1}{2}\varepsilon_{ijk}u_{j,i} \tag{7b}$$

Taking the gradient of the rotation field and only considering the skew-symmetric contribution, we are left with the mean curvature tensor

$$\kappa_{ij} = \omega_{[i,j]} = \frac{1}{2}(\omega_{i,j} - \omega_{j.i}) \tag{8}$$

Because this mean curvature tensor is skew-symmetric, it can be represented as a polar vector through the following duality relation

$$\kappa_i = \frac{1}{2}\varepsilon_{ijk}\kappa_{kj} \tag{9}$$

From classical linear elasticity theories we know that the strain contributes to the overall elastic potential energy, however in Hadjesfandiari and Dargush (2011) it is shown that mean curvature is the second suitable measure of deformation, which also contributes to the elastic potential energy. Indeed, it is shown that the mean curvature tensor is the energy conjugate quantity to the couple-stress tensor for a consistent couple-stress theory. Other past theories have concluded that the strain-gradient or other higher order kinematic quantities should be considered. However, this has been shown in Hadjesfandiari and Dargush (2011) to be incorrect by considering admissible boundary conditions and virtual work applied to an arbitrary continuum material element. The

important consequence of this discovery is the skew-symmetric nature of the couple-stress tensor, which makes the theory fully determinate.

Because the couple-stress tensor is skew-symmetric, it also has a corresponding dual polar vector μ_i, where

$$\mu_i = \frac{1}{2}\varepsilon_{ijk}\mu_{kj} \tag{10}$$

From (2), the skew-symmetric portion of the force-stress tensor is related to the couple-stress by

$$\sigma_{[ji]} = -\mu_{[i,j]} = -\frac{1}{2}\left(\mu_{i,j} - \mu_{j,i}\right) \tag{11}$$

Naturally, this skew-symmetric portion can be represented as a pseudo vector s_i as well, such that

$$s_i = \frac{1}{2}\varepsilon_{ijk}\sigma_{[kj]} \tag{12a}$$

and

$$\varepsilon_{ijk}s_k = \sigma_{[ji]} \tag{12b}$$

For force-stress, we have the obvious decomposition

$$\sigma_{ji} = \sigma_{(ji)} + \sigma_{[ji]} \tag{13a}$$

which, after substituting Eq. (12b), may be written

$$\sigma_{ji} = \sigma_{(ji)} + \varepsilon_{ijk} s_k \tag{13b}$$

Furthermore, substituting (13b) into (1) and (12a) into (2) yields the following alternate relations for linear and angular momentum balance

$$\sigma_{(ji),j} + \varepsilon_{ijk} s_{k,j} + \bar{F}_i = 0 \tag{14a}$$

$$\mu_{ji,j} + 2s_i = 0 \tag{14b}$$

Based upon the development in Hadjesfandiari and Dargush (2011) we may write the elastic energy density for a linear, isotropic couple stress material as

$$U(e, \kappa) = \frac{1}{2} c_{ijkl} e_{ij} e_{kl} + \frac{1}{2} b_{ijkl} \kappa_{ij} \kappa_{kl} \tag{15}$$

in terms of the tensorial strain e_{ij} and mean curvature κ_{ij}. In (15), c_{ijkl} is the standard 4th order constitutive tensor used for classical linear elasticity theories, which in the isotropic case depends on two elastic constants, for example, the Lamé constants λ and μ. Meanwhile, b_{ijkl} is the 4th order linear couple-stress constitutive tensor.

In the present work, we will also deal with energy conjugate mean curvature and couple-stress polar vectors. Consequently, we define the engineering mean curvature k_i, such that

$$k_i = -2\kappa_i = \varepsilon_{ijk} \kappa_{jk} \tag{16}$$

With this definition, the components of the engineering mean curvature, k_1, k_2, and k_3, at any point *P,* are the mean curvature of planes parallel to the x_2x_3, x_3x_1 and x_1x_2-planes, respectively, at that point.

For the elastic energy density, we may write

$$U(e,k) = \frac{1}{2}c_{ijkl}e_{ij}e_{kl} + \frac{1}{2}b_{ij}k_ik_j \tag{17}$$

with constitutive tensor b_{ij}.

From the internal energy density equation (15), the constitutive relations for symmetric force-stress and couple-stress can be derived, respectively, as follows:

$$\sigma_{(ji)} = \frac{\partial U}{\partial e_{ij}} = c_{ijkl}e_{kl} \tag{18}$$

$$\mu_{ji} = \frac{\partial U}{\partial \kappa_{ij}} = b_{ijkl}\kappa_{kl} \tag{19a}$$

while the vector form of couple stress can be related to the internal energy from (17) by

$$\mu_i = \frac{\partial U}{\partial k_i} = b_{ij}k_j \tag{19b}$$

and the two couple-stress constitutive tensors are related by

$$b_{lmrs} = \varepsilon_{ilm}\varepsilon_{jrs}b_{ij} \tag{20}$$

Equation (19b) tells us that the couple-stress vector μ_i and engineering mean curvature vector k_i are indeed the correct energy conjugate vector quantities. This form is more convenient than in Hadjesfandiari and Dargush (2011), where use of the dual curvature vector κ_i requires introduction of a factor of minus two within the energy conjugacy relations. This is the underlying reason for introducing k_i here, as the engineering mean curvature vector. Furthermore, the components of k_i are consistent with the usual mathematical definition of mean curvatures of the three orthogonal planes oriented with the global axes at a point.

From Hadjesfandiari and Dargush (2011), only one additional material property, η, is necessary to form the couple stress constitutive tensor for an isotropic material. For the simple case of linear elasticity in an isotropic material, we have

$$b_{lmrs} = 4\eta(\delta_{lr}\delta_{ms} - \delta_{ls}\delta_{mr}) \tag{21}$$

$$b_{ij} = 4\eta\delta_{ij} \tag{22}$$

Interestingly, we find that there is a characteristic length l associated with such materials, defined by the relationship

$$\frac{\eta}{\mu} = l^2 \tag{23a}$$

for isotropic materials, and

$$\frac{\eta}{c_{44}} = l^2 \tag{23b}$$

for cubic crystals with centrosymmetry. It is expected that couple-stress effects, and in the following chapter, size-dependent piezoelectric effects, are only relevant for length scales comparable to l.

2.2 Couple Stress Variational Formulation

The goal here is to develop a variational formulation for a couple-stress solid that has linear and angular momentum balances, as well as the natural boundary conditions as its resulting Euler-Lagrange equations and only requires C^0 continuity of the field variables. In order to relax continuity requirements, we consider rotation to be independent from displacement and then enforce rotation-displacement compatibility through the use of Lagrange multipliers. It is shown that this formulation has the interesting advantage that these Lagrange multipliers are equal to the skew-symmetric stress, which otherwise would be difficult to calculate. Because of these aforementioned advantages, this formulation is a very convenient starting point for developing numerical methods, specifically FEM formulations (Bathe, 2006; Zienkiewicz and Taylor, 2000), such as the one to be presented here.

Consider the following total energy functional that includes the internal elastic energy and the potential energy from applied forces

$$\Pi = \frac{1}{2}\int_V e_{ij} c_{ijkl} e_{kl}\, dV + \frac{1}{2}\int_V \kappa_{ij} b_{ijkl} \kappa_{kl}\, dV - \int_V u_i \bar{F}_i\, dV - \int_{S_t} u_i \bar{t}_i\, dS - \int_{S_m} \omega_i \bar{m}_i\, dS \tag{24}$$

Recall that the overbars denote applied forces and moments, which consequently are not subject to variation.

In the couple stress continuum problem, both strain and curvature are functions of the displacement field, such that

$$\Pi \equiv \Pi(e(u), \kappa(u), u) \tag{25}$$

We now can extremize this functional by taking the first variation and setting that equal to zero. However, this would require C^1 continuity of the displacement field.

Alternatively, we may consider independent displacements and rotations and then enforce the rotation-displacement compatibility constraint (7b) by incorporating Lagrange multipliers into our original energy functional prior to taking the variation. Thus, we may define a new functional

$$\widetilde{\Pi} \equiv \widetilde{\Pi}(e(u), \kappa(\omega), u, \omega, \lambda) \tag{26}$$

where

$$\widetilde{\Pi} = \Pi + \int_V \lambda_k \left(\varepsilon_{kji} u_{i,j} - 2\omega_k\right) dV \tag{27}$$

and finally

$$\begin{aligned} \widetilde{\Pi} = \frac{1}{2}\int_V e_{ij} c_{ijkl} e_{kl}\, dV + \frac{1}{2}\int_V \kappa_{ij} b_{ijkl} \kappa_{kl}\, dV + \int_V \lambda_k \left(\varepsilon_{kji} u_{i,j} - 2\omega_k\right) dV \\ - \int_V u_i \bar{F}_i\, dV - \int_{S_t} u_i \bar{t}_i\, dS - \int_{S_m} \omega_i \bar{m}_i\, dS \end{aligned} \tag{28}$$

where the components of λ_i are the Lagrange multipliers. After some maneuvers, we will show that these Lagrange multipliers λ_i are equal to the skew-symmetric stress vector s_i.

We now consider the stationarity of this functional in order to find the static equilibrium solution by equating the first variation to zero. With a bit of mathematical manipulation, we will show that the solutions emanating from this process are identical to the solutions that satisfy the governing partial differential equations for our system, as well as the natural boundary conditions. In other words, the resulting Euler-Lagrange equations represent linear momentum balance, angular momentum balance, rotation-displacement compatibility, and both the force- and moment-traction boundary conditions.

For the stationarity of $\widetilde{\Pi}$, we enforce its first variation in (28) to be zero, that is

$$\delta\widetilde{\Pi} = \frac{\partial \widetilde{\Pi}}{\partial u_i}\delta u_i + \frac{\partial \widetilde{\Pi}}{\partial \omega_i}\delta \omega_i + \frac{\partial \widetilde{\Pi}}{\partial \lambda_i}\delta \lambda_i = 0 \tag{29}$$

This can be written as

$$\delta\widetilde{\Pi} = \int_V \left(c_{ijkl}e_{kl} + \varepsilon_{kji}\lambda_k\right)\delta u_{i,j}\, dV + \int_V b_{ijkl}\kappa_{kl}\delta\omega_{i,j}\, dV - 2\int_V \lambda_i\delta\omega_i dV$$
$$+ \int_V \delta\lambda_k\left(\varepsilon_{kji}u_{i,j} - 2\omega_k\right)dV \tag{30}$$
$$+ \int_V \delta u_i\bar{F}_i\, dV - \int_{S_t} \delta u_i\bar{t}_i\, dS - \int_{S_m} \delta\omega_i\bar{m}_i\, dS = 0$$

where the symmetric character of c_{ijkl} and b_{ijkl} has been used to simplify the first and second terms. Considering the product rule we can rewrite the first two integrals in (30), such that

$$\delta\widetilde{\Pi} = \int_V \left[\left(c_{ijkl}e_{kl} + \varepsilon_{kji}\lambda_k\right)\delta u_i\right]_{,j} dV - \int_V \left[\left(c_{ijkl}e_{kl} + \varepsilon_{kji}\lambda_k\right)_{,j} + \bar{F}_i\right]\delta u_i\, dV$$
$$+ \int_V \left(b_{ijkl}\kappa_{kl}\delta\omega_i\right)_{,j} dV - \int_V \left[\left(b_{ijkl}\kappa_{kl}\right)_{,j} + 2\lambda_i\right]\delta\omega_i dV \tag{31}$$
$$+ \int_V \delta\lambda_k\left(\varepsilon_{kji}u_{i,j} - 2\omega_k\right)dV - \int_{S_t} \delta u_i\bar{t}_i\, dS - \int_{S_m} \delta\omega_i\bar{m}_i\, dS = 0$$

Now we apply the divergence theorem to the first and third volume integrals and obtain the relation

$$\delta\widetilde{\Pi} = \int_{S_t} \left[\left(c_{ijkl}e_{kl} + \varepsilon_{kji}\lambda_k\right)n_j - \bar{t}_i\right]\delta u_i\, dS - \int_V \left[\left(c_{ijkl}e_{kl} + \varepsilon_{kji}\lambda_k\right)_{,j} + \bar{F}_i\right]\delta u_i\, dV$$
$$+ \int_{S_m} \left[b_{ijkl}\kappa_{kl}n_j - \bar{m}_i\right]\delta\omega_i\, dS - \int_V \left[\left(b_{ijkl}\kappa_{kl}\right)_{,j} + 2\lambda_i\right]\delta\omega_i dV \tag{32}$$
$$+ \int_V \delta\lambda_k\left(\varepsilon_{kji}u_{i,j} - 2\omega_k\right)dV = 0$$

where the conditions $\delta u_i = 0$ on S_u and $\delta\omega_i = 0$ on S_ω have been used.

Because the variations δu_i, $\delta \omega_i$, and $\delta \lambda_i$ are independent and arbitrary in the domain V and the boundary surfaces S_t and S_m, each individual term in the integrals must vanish separately. Therefore, we have

$$\left(c_{ijkl} e_{kl} + \varepsilon_{kji} \lambda_k\right)_{,j} + \bar{F}_i = 0 \quad \text{in } V \tag{33}$$

$$\left(b_{ijkl} \kappa_{kl}\right)_{,j} + 2\lambda_i = 0 \quad \text{in } V \tag{34}$$

$$\omega_k = \frac{1}{2} \varepsilon_{ijk} u_{j,i} \quad \text{in } V \tag{35}$$

$$\bar{t}_i = \left(c_{ijkl} e_{kl} + \varepsilon_{kji} \lambda_k\right) n_j \quad \text{on } S_t \tag{36}$$

$$\bar{m}_i = b_{ijkl} \kappa_{kl} n_j \quad \text{on } S_m \tag{37}$$

Equations (33) and (34) are the equilibrium equations (1) and (2), where

$$\sigma_{(ji)} = c_{ijkl} e_{kl} \tag{38}$$

$$\sigma_{[ji]} = \lambda_k \varepsilon_{kji} \tag{39}$$

$$\mu_{ji} = b_{ijkl} \kappa_{kl} \tag{40}$$

$$\varepsilon_{ijk} \sigma_{jk} = 2\lambda_i \tag{41}$$

By comparing (41) and (12a), we obtain

$$\lambda_i = s_i \quad \text{in } V \tag{42}$$

This result is of importance theoretically and also because calculating the skew-symmetric stress otherwise would be a non-trivial task, involving higher order derivatives.

Meanwhile, equations (36) and (37) yield the natural boundary conditions (3a) and (3b), respectively.

We have now shown that the variational principle associated with the stationarity of (28) is valid for couple stress isotropic elasticity. The solutions obtained from (29) will satisfy both linear and angular equilibrium, as well as the natural boundary conditions. Furthermore, the Lagrange multiplier vector was shown to be equal to the skew-symmetric stress vector. Note that the formulation developed here is in terms of the vector forms of rotation and skew-symmetric stress. This is for convenience and uniformity of variables; however, we could also consider the same type of formulation in terms of the respective tensor form of these variables.

2.3 Couple Stress Finite Element Formulation

In order to take full advantage of the recent advances in couple-stress theory reviewed here, numerical methods must be explored. Here we develop a FEM formulation that will include couple-stress effects.

For the purpose of simplifying calculations and programming, Voigt notation is used. This means that the strain, $\boldsymbol{e}$, can be represented by a vector rather than a second order tensor, and the constitutive tensor, $\boldsymbol{c}$, can be represented by a two-dimensional matrix rather than a fourth order tensor. For the two-dimensional, plane-strain, linear, isotropic problems that we will explore here we then have the following relations

$$\boldsymbol{e} = \begin{bmatrix} e_{xx} \\ e_{yy} \\ \gamma_{xy} \end{bmatrix} = \begin{bmatrix} \frac{\partial u_x}{\partial x} \\ \frac{\partial u_y}{\partial y} \\ \frac{\partial u_x}{\partial y} + \frac{\partial u_y}{\partial x} \end{bmatrix} \tag{43}$$

$$\boldsymbol{c} = \frac{E(1-\nu)}{(1+\nu)(1-2\nu)} \begin{bmatrix} 1 & \frac{\nu}{1-\nu} & 0 \\ \frac{\nu}{1-\nu} & 1 & 0 \\ 0 & 0 & \frac{1-2\nu}{2(1-\nu)} \end{bmatrix} \tag{44}$$

where u_x is the component of displacement in the x-direction and u_y is the component of the displacement in the y-direction. Additionally, E is the Young's modulus, and ν is the Poisson's ratio. For plane-stress problems the only thing that will change is $\boldsymbol{c}$ (Bathe, 2006; Zienkiewicz and Taylor, 2000).

For planar problems, the engineering mean curvature in vector form can be written in terms of the one out of plane component of rotation explicitly as

$$\boldsymbol{k} = \begin{bmatrix} k_x \\ k_y \end{bmatrix} = \begin{bmatrix} -\frac{\partial \omega}{\partial y} \\ \frac{\partial \omega}{\partial x} \end{bmatrix} \tag{45}$$

where $\omega = \omega_z$ and the couple-stress constitutive matrix for a linear isotropic material is

$$\boldsymbol{b} = 4\eta \begin{bmatrix} 1 & 0 \\ 0 & 1 \end{bmatrix} \tag{46}$$

We now reconsider the variational principle developed in the preceding section. In vector notation we have

$$\delta \widetilde{\Pi} = \frac{\partial \widetilde{\Pi}}{\partial \boldsymbol{u}} \delta \boldsymbol{u} + \frac{\partial \widetilde{\Pi}}{\partial \boldsymbol{\omega}} \delta \boldsymbol{\omega} + \frac{\partial \widetilde{\Pi}}{\partial \boldsymbol{s}} \delta \boldsymbol{s} = 0 \tag{47}$$

where

$$\widetilde{\Pi} = \frac{1}{2}\int_V \boldsymbol{e}^T \boldsymbol{c}\boldsymbol{e}\, dV + \frac{1}{2}\int_V \boldsymbol{k}^T \boldsymbol{b}\boldsymbol{k}\, dV + \int_V (curl\, \boldsymbol{u} - 2\boldsymbol{\omega})^T\, \boldsymbol{s}\, dV$$

$$- \int_V \boldsymbol{u}^T \overline{\boldsymbol{F}}\, dV - \int_{S_t} \boldsymbol{u}^T \bar{\boldsymbol{t}}\, dS - \int_{S_m} \boldsymbol{\omega}^T \overline{\boldsymbol{m}}\, dS \tag{48}$$

This mixed formulation has additional degrees of freedom when compared to a pure displacement based formulation, namely rotation and skew-symmetric stress, but only requires C^0 continuity for displacement.

Now consider discretizing our domain into a finite number of elements. In particular 8-node quadratic elements are used in this formulation. The reason for not considering simpler four node elements is that the linear elements have increased difficulty in terms of maintaining rotation-displacement compatibility when compared to higher order elements.

Figure 1 shows a standard 8-node isoparametric quadrilateral master element. This element has natural coordinates represented by r and s, with values for each element ranging from -1 to +1 in either direction. In the global coordinate system, here represented in two dimensions by Cartesian coordinates x and y, our element can take on any arbitrary shape so long as the distortion of the geometry is not too extreme (Bathe, 2006; Zienkiewicz and Taylor, 2000).

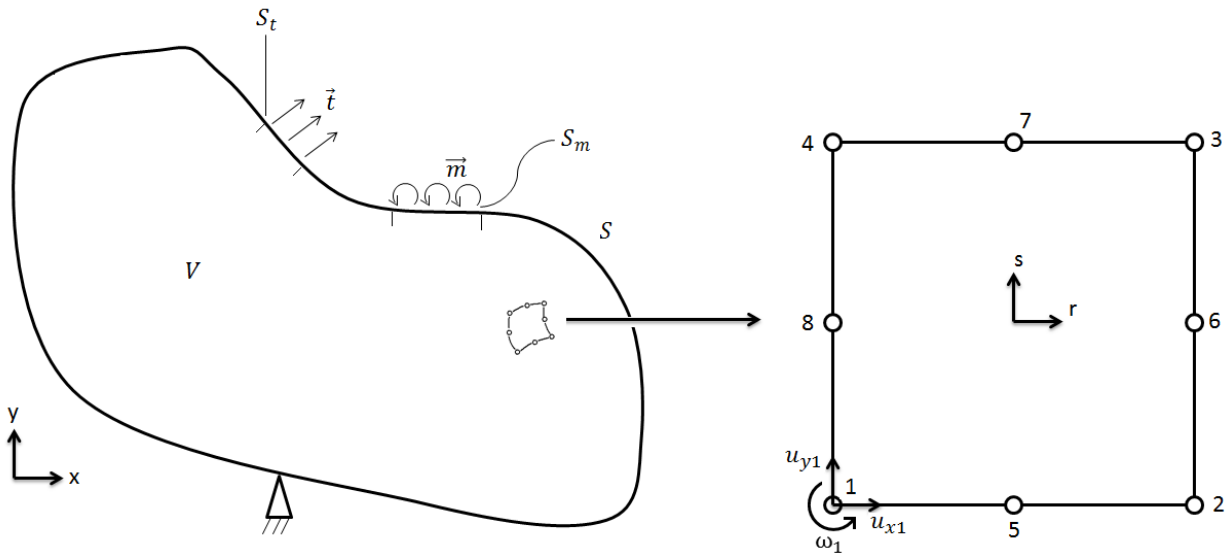

Fig. 1. General two-dimensional body and 8-node isoparametric master element

Standard serendipity quadratic shape functions $\boldsymbol{N}$ (Bathe, 2006; Zienkiewicz and Taylor, 2000) are used in this formulation, where for completeness of presentation,

$$\boldsymbol{N}^T = \begin{bmatrix} \frac{1}{4}(1-r)(1-s) - \frac{1}{4}(1-s^2)(1-r) - \frac{1}{4}(1-r^2)(1-s) \\ \frac{1}{4}(1+r)(1-s) - \frac{1}{4}(1-r^2)(1-s) - \frac{1}{4}(1-s^2)(1+r) \\ \frac{1}{4}(1+r)(1+s) - \frac{1}{4}(1-r^2)(1+s) - \frac{1}{4}(1-s^2)(1+r) \\ \frac{1}{4}(1-r)(1+s) - \frac{1}{4}(1-r^2)(1+s) - \frac{1}{4}(1-s^2)(1-r) \\ \frac{1}{2}(1-s)(1-r^2) \\ \frac{1}{2}(1+r)(1-s^2) \\ \frac{1}{2}(1+s)(1-r^2) \\ \frac{1}{2}(1-r)(1-s^2) \end{bmatrix} \tag{49}$$

These same shape functions $\boldsymbol{N}$ are used to interpolate both the geometric coordinates of the element as well as the displacement and rotation field variables within the element. This means that we represent the geometry of an arbitrary shaped element in terms of the natural coordinates r and s via the following relations:

$$x \cong \boldsymbol{N}\hat{\boldsymbol{x}} \tag{50a}$$

$$y \cong \boldsymbol{N}\hat{\boldsymbol{y}} \tag{50b}$$

where $\hat{\boldsymbol{x}}$ and $\hat{\boldsymbol{y}}$ are the global coordinate values of nodes 1 through 8 for any particular element. We can then use these same shape functions to approximate the unknown displacement and rotation fields as follows:

$$u_x \cong \boldsymbol{N}\hat{\boldsymbol{u}}_{\boldsymbol{x}} \tag{51a}$$

$$u_y \cong \boldsymbol{N}\hat{\boldsymbol{u}}_{\boldsymbol{y}} \tag{51b}$$

$$\omega \cong \boldsymbol{N}\hat{\boldsymbol{\omega}} \tag{51c}$$

with similar relations to represent the corresponding variations. In general the hat notation is used to represent vectors containing quantities at nodes 1 through 8. For example, $\widehat{\boldsymbol{\omega}}$ is a vector of length 8 containing the nodal values of planar rotation for a particular element.

For the displacements and rotations on the boundaries S_t and S_m, we use surface interpolation functions, such that

$$u_{xS_t} \cong \boldsymbol{N}_S \widehat{\boldsymbol{u}}_{\boldsymbol{x}} \tag{52a}$$

$$u_{yS_t} \cong \boldsymbol{N}_S \widehat{\boldsymbol{u}}_{\boldsymbol{y}} \tag{52b}$$

$$\omega_{S_m} \cong \boldsymbol{N_S} \widehat{\boldsymbol{\omega}} \tag{52c}$$

For a 2-d body these surface shape functions are only one-dimensional in terms of the natural coordinates. The surface shape functions we use here are

$$\boldsymbol{N_S^T} = \begin{bmatrix} \frac{1}{2}(1-r) - \frac{1}{2}(1-r^2) \\ \frac{1}{2}(1+r) - \frac{1}{2}(1-r^2) \\ 1-r^2 \end{bmatrix} \tag{53}$$

Next we replace the strains and curvatures in (48) with approximate discrete representations in terms of displacements and rotations. To do this we must introduce new matrices, the strain-displacement matrix, $\boldsymbol{B_e}$, such that

$$\boldsymbol{e} \cong \boldsymbol{B_e} \widehat{\boldsymbol{u}} \tag{54}$$

the curvature-rotation matrix, $\boldsymbol{B_k}$, such that

$$\boldsymbol{k} \cong \boldsymbol{B_k}\widehat{\boldsymbol{\omega}} \tag{55}$$

and finally the curl-displacement matrix, such that

$$\nabla \times \boldsymbol{u} \cong \boldsymbol{B_{curl}}\widehat{\boldsymbol{u}} \tag{56}$$

For the planar problems we consider in this thesis, we can write out these $\boldsymbol{B}$ matrices explicitly as follows:

$$\boldsymbol{B_e} = \begin{bmatrix} \frac{\partial N_1}{\partial x} & 0 & & \frac{\partial N_8}{\partial x} & 0 \\ 0 & \frac{\partial N_1}{\partial y} & \dots & 0 & \frac{\partial N_8}{\partial y} \\ \frac{\partial N_1}{\partial y} & \frac{\partial N_1}{\partial x} & & \frac{\partial N_8}{\partial y} & \frac{\partial N_8}{\partial x} \end{bmatrix} \tag{57a}$$

$$\boldsymbol{B_k} = \begin{bmatrix} -\frac{\partial N_1}{\partial y} & \dots & -\frac{\partial N_8}{\partial y} \\ \frac{\partial N_1}{\partial x} & & \frac{\partial N_8}{\partial x} \end{bmatrix} \tag{57b}$$

$$\boldsymbol{B_{curl}} = \begin{bmatrix} -\frac{\partial N_1}{\partial y} & \frac{\partial N_1}{\partial x} & \dots & -\frac{\partial N_8}{\partial y} & \frac{\partial N_8}{\partial x} \end{bmatrix} \tag{57c}$$

Here $\boldsymbol{B_e}$ is a matrix of size [3x16], $\boldsymbol{B_k}$ is of size [2x8], while the matrix $\boldsymbol{B_{curl}}$ is of size [1x16]. Note that $\boldsymbol{B_e}$ and $\boldsymbol{B_{curl}}$ operate on an extended displacement vector that includes both x and y components. When considering (57a) and (57c), we have

$$\widehat{\boldsymbol{u}}^T = [\widehat{\boldsymbol{u}}_{\boldsymbol{x}}, \widehat{\boldsymbol{u}}_{\boldsymbol{y}}] = [\, \hat{u}_{x1} \quad \hat{u}_{y1} \quad \dots \quad \hat{u}_{x8} \quad \hat{u}_{y8} \,] \tag{58}$$

In all cases, the $\boldsymbol{B}$ matrices above are functions of the first derivatives of our shape functions with respect to global Cartesian coordinates x and y. Of course, in order to obtain derivatives of the shape functions with respect to global coordinates, we first take derivatives with respect to natural coordinates, r and s, and then multiply by the inverse of the Jacobian, $\boldsymbol{J}$, where

$$\boldsymbol{J} = \begin{bmatrix} \frac{\partial x}{\partial r} & \frac{\partial y}{\partial r} \\ \frac{\partial x}{\partial s} & \frac{\partial y}{\partial s} \end{bmatrix} \tag{59}$$

Finally, we must also consider the discrete approximation of the skew-symmetric stress pseudo vector. For 2-d problems this vector actually simplifies to one component in the out of plane direction. Further simplifying matters, we need only C^{-1} continuity in this formulation and therefore consider $\boldsymbol{s}$ to be constant throughout each element.

Now, upon substitution of the discrete representations of our variables into (48), and then taking the first variation with respect to the discrete variables, we are left with the following for each element

$$\begin{aligned} \delta\widetilde{\Pi} = (\delta\widehat{\boldsymbol{u}})^T & \left[\int_V (\boldsymbol{B}^T\boldsymbol{c}\boldsymbol{B})\,\widehat{\boldsymbol{u}}\,J_d dV + \int_V \boldsymbol{B_{curl}}^T\,\boldsymbol{s}\,J_d\,dV - \int_V \boldsymbol{N}^T\overline{\boldsymbol{F}}\,J_d dV - \int_{S_t} \boldsymbol{N}_S^T\,\bar{\boldsymbol{t}}\,J_{dS}\,dS\right] \\ & + (\delta\widehat{\boldsymbol{\omega}})^T\left[\int_V (\boldsymbol{B}_{\boldsymbol{k}}^T\boldsymbol{b}\boldsymbol{B}_{\boldsymbol{k}})\,\widehat{\boldsymbol{\omega}}\,J_d dV + \int_V -2\boldsymbol{N}^T\boldsymbol{s}\,J_d dV - \int_{S_m} \boldsymbol{N}_S^T\,\overline{\boldsymbol{m}}\,J_{dS}\,dS\right] \\ & + (\delta s)\left[\int_V (\boldsymbol{B_{curl}}\widehat{\boldsymbol{u}} - 2\boldsymbol{N}\widehat{\boldsymbol{\omega}})\,J_d dV\right] = 0 \end{aligned} \tag{60}$$

where J_d and J_{dS} represent the determinants of the Jacobian of the volume and the surface of an element, respectively. For the integration over the 8-noded isoparametric couple-stress elements presented here, standard 3x3 point Gauss quadrature is used (Bathe, 2006; Zienkiewicz and Taylor, 2000).

Due to the fact that the variational factors, $\delta\widehat{\boldsymbol{u}}$, $\delta\widehat{\boldsymbol{\omega}}$, and $\delta\boldsymbol{s}$ have arbitrary value, the three terms in square brackets above all must be identically zero for this equation to be valid. This provides us with three coupled sets of linear algebraic equations for each element. These are our final individual finite element equations in matrix form.

We have now a set of linear algebraic equations for each element. Here we choose to organize these element equations into the standard form shown in Fig. 2.

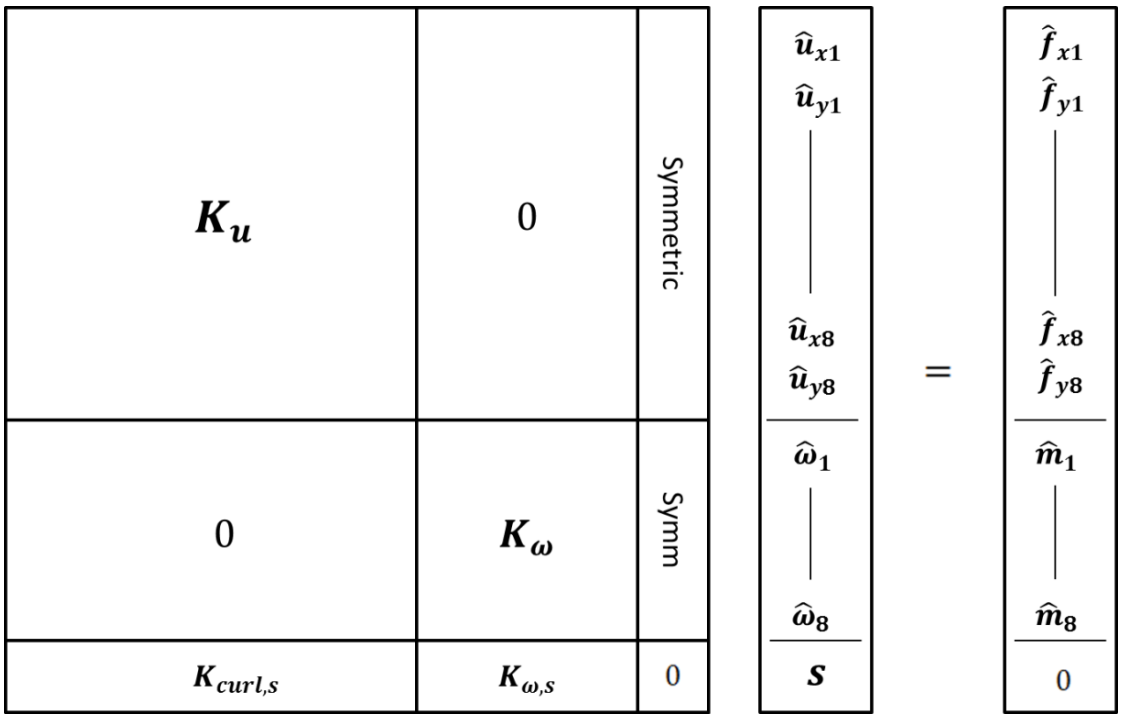

Fig. 2. Structure of resulting element equations before assembly

The stiffness terms on the left hand side are calculated as follows:

$$\boldsymbol{K_u} = \int_V \left(\boldsymbol{B_e}^T \boldsymbol{c} \boldsymbol{B_e}\right) J_d dV \tag{61a}$$

$$\boldsymbol{K_\omega} = \int_V (\boldsymbol{B_k^T} \boldsymbol{b} \boldsymbol{B_k})\, J_d dV \tag{61b}$$

$$\boldsymbol{K_{curl,s}} = \int_V (\boldsymbol{B_{curl}})\, J_d dV \tag{61c}$$

$$\boldsymbol{K_{\omega,s}} = \int_V (-2\boldsymbol{N})\, J_d dV \tag{61d}$$

For the right hand side, we have

$$\hat{\boldsymbol{f}}_{\boldsymbol{x}} = \int_V \boldsymbol{N}^T \bar{F}_x \, J_d dV + \int_{S_t} \boldsymbol{N}_S^T \, \bar{t}_x \, J_{dS} \, dS \tag{62a}$$

$$\hat{\boldsymbol{f}}_{\boldsymbol{y}} = \int_V \boldsymbol{N}^T \bar{F}_y \, J_d dV + \int_{S_t} \boldsymbol{N}_S^T \, \bar{t}_y \, J_{dS} \, dS \tag{62b}$$

$$\hat{\boldsymbol{m}} = \int_{S_m} \boldsymbol{N}_S^T \, \bar{m} \, J_{dS} \, dS \tag{62c}$$

where the subscripts x and y above indicate the components of force and traction in that respective direction. All terms that appear in the right hand side are of course known quantities.

After evaluating the stiffness matrix and forcing vector on the element level, we then follow standard finite element procedures to assemble and solve the global set of linear algebraic equations

$$\boldsymbol{K}\boldsymbol{u} = \boldsymbol{f} \tag{63}$$

where now $\boldsymbol{u}$ includes displacements, rotations and skew-symmetric stresses.

Before examining several applications of the consistent couple stress FE formulation in the next section, a simple patch test is performed to show that indeed the elements used here are viable. Consider the performance of the square mesh with distorted elements shown in Fig. 3 with material parameters $E = 5/2,\ \nu = 1/4$ and $l = 1$. First, the displacement boundary conditions corresponding to rigid body states are imposed on the edge nodes of the patch. Thus, displacement boundary conditions are enforced at every boundary node corresponding to a unit rigid body translation in the x- and y- directions.

This of course should result in zero stress and strain within the body for both cases. The error in the resulting stress and strain fields was less than 10^{-14}. Next, displacement boundary conditions corresponding to a constant rotation state were enforced by specifying boundary conditions, such that $\omega = (u_{y,x} - u_{x,y})/2 = 1$. Again, the error in the resulting stress and strain fields was less than 10^{-14}. Finally, a constant strain and stress state was enforced on all edges of the mesh in Fig. 3. The specific conditions were defined for a stress state with $\sigma_{xx} = 2$ and $\sigma_{yy} = \sigma_{xy} = 0$ to exist everywhere within the body. The resulting stress and strain fields from enforcing the boundary conditions compatible with this constant strain and stress state were accurate everywhere in the body to within machine precision. More specifically the maximum values of error for all stresses and strains, when compared to the analytical solution, were less than 10^{-14}.

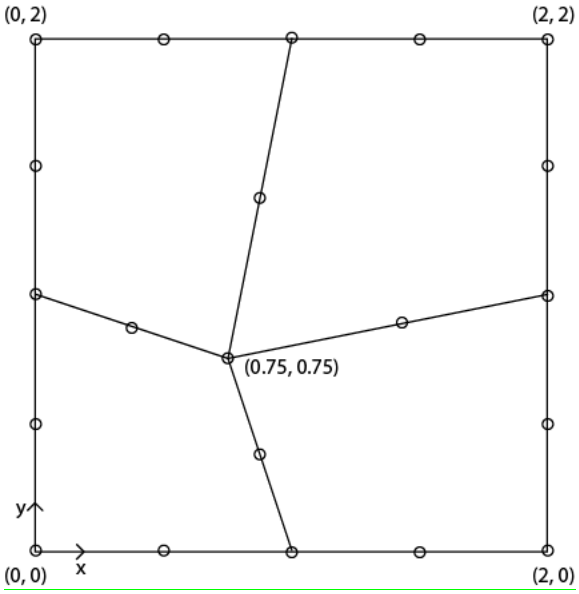

Fig. 3. Mesh used for patch test

2.4 Size-dependent Elasticity Problems

2.4.1 *Uniform Traction on Plate with Circular Hole*

The first example we consider is that of a circular hole in a plate using plane-strain assumptions. Previously, Mindlin (1963) studied stress concentration factors for this problem within the inconsistent couple stress theory.

Symmetry considerations allow us to simplify the problem geometry to a quarter plate, as shown in Fig. 4. We consider dimensions $a = b = 1$ and uniform traction, $t_0 = 1/2$. The material properties are taken in non-dimensional form, as $E = 5/2$ and $\nu = 1/4$, to provide a shear modulus of unity.

Referring to Fig. 4 the boundary conditions for this problem are as follows. The top surface and the circular surface are both traction-free. The left surface has zero horizontal displacement, zero vertical traction, and zero rotation. The bottom surface has zero vertical displacement, zero horizontal traction, and zero rotation, whereas the right side is subject to uniform horizontal traction t_0.

The results are tabulated for various values of the couple stress parameter, η, which in this case is equal to l^2/a^2, in Table 1 below. Increasing values of l^2/a^2 can be seen as decreasing the characteristic geometry of the problem. Here U_{CL} is the horizontal displacement at the centerline, or the bottom right corner in Fig. 4, U_{TC} is the horizontal displacement at the top right corner, and SCF is the stress concentration factor for this structure at the top of the hole. We see that these results are in excellent agreement with the boundary element results from Hadjesfandiari and Dargush (2011).

For this problem the smallest value of $l^2/a^2 = 1 \times 10^{-8}$ essentially yields the same solution as the classical plane-strain solution. We see that by increasing this parameter the effect of including couple-stress effects causes significant deviation from the classical solution. Most interesting is the sharp decrease of the stress concentration factor with increasing value of the couple stress parameter.

Figures 5a and 5b show contours of the axial stress and the deformed configuration for the case of classical elasticity and couple-stress elasticity with $l^2/a^2 = 1$, respectively. It is clear that the effect of couple-stresses is to decrease the bending deformation and smooth out the axial stress field. Interestingly, one could predict that with increasing dominance of couple-stress effects the solution actually becomes purely axial and the stress concentration factor goes to unity.

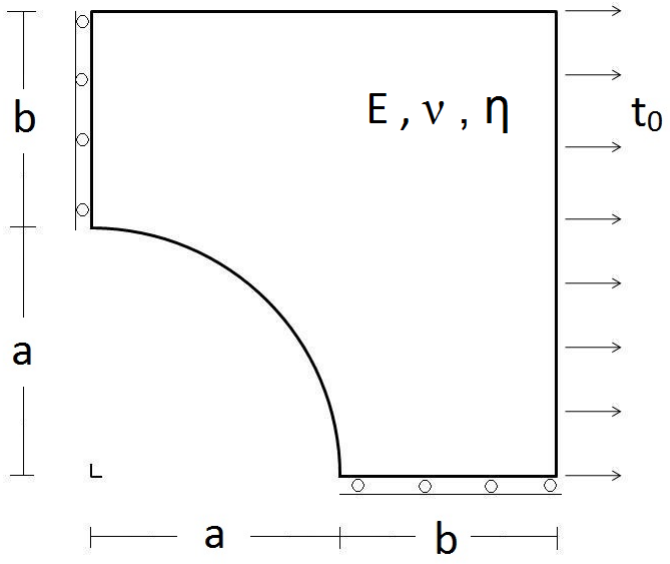

Fig. 4. Problem schematic of hole in finite plate

Table 1. Results for hole in a finite plate

	$\frac{l^2}{a^2}$	**BEM 160 elements**	FEM 12 elements	FEM 133 elements	**FEM 841 elements**
$\mathbf{U_{CL}}$	1.00E-08	1.4634	1.4436	1.4615	1.4634
	0.0625	0.9387	0.9527	0.9362	0.9388
	0.25	0.7051	0.7133	0.7030	0.7051
	1	0.6038	0.6091	0.6022	0.6039
$\mathbf{U_{TC}}$	1.00E-08	0.1464	0.1493	0.1465	0.1464
	0.0625	0.3557	0.3547	0.3559	0.3557
	0.25	0.4617	0.4646	0.4619	0.4617
	1	0.5102	0.5158	0.5102	0.5102
SCF	1.00E-08	3.1935	3.1073	3.2080	3.1948
	0.0625	2.0058	1.9438	2.0165	2.0056
	0.25	1.4998	1.4360	1.5072	1.5000
	1	1.2866	1.2265	1.2931	1.2869

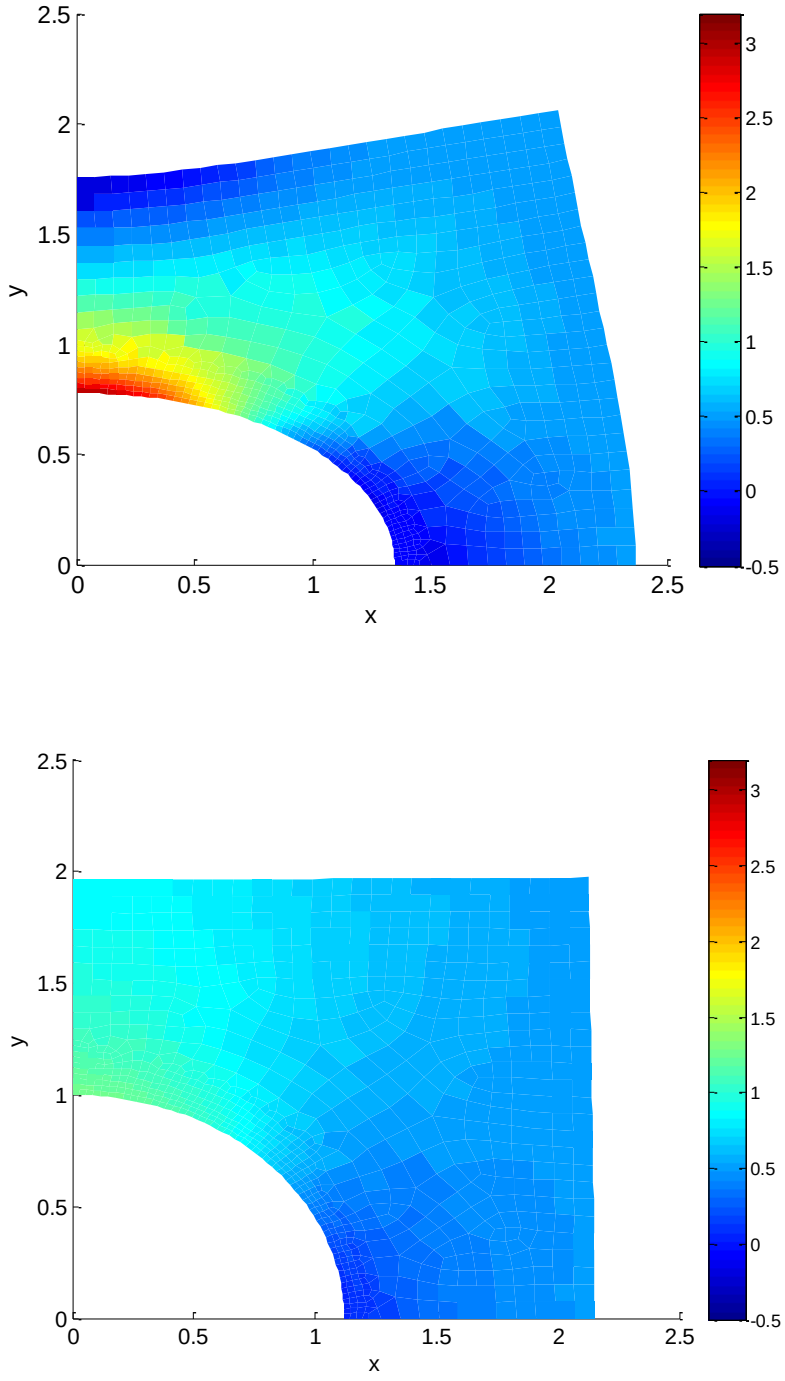

Fig. 5. Contours of σ_{xx} and deformed geometry (deformation scaled by factor of 0.25)

(a) Case 1: Classical elasticity;

(b) Case 2: Couple-stress elasticity, l^2/a^2.

2.4.2 *Deformation of Plane Ring*

The second example considered is the deformation of a ring, as shown in Fig. 6, using plane strain assumptions. The deformation is a unit displacement of the inner surface in the positive x- direction. Again for material properties we use $E = 5/2$ and $\nu = 1/4$. The inner surface has radius $a = 1$ and the outer surface has radius $b = 2$. Point A is located at $r = a$ and $\theta = \pi/2$, while Point B is located at $r = b$ and $\theta = \pi/2$.

The boundary conditions are as follows: on the outer surface we have zero displacement, while on the inner surface a unit horizontal displacement ($U = 1$) is enforced as well as zero vertical displacement. There are no applied tractions or body forces.

There is an analytical solution available for this particular problem from Hadjesfandiari and Dargush (2011). For the finite element analysis, an unstructured mesh consisting of 2,900 elements was used with refinement about point A. Figures 7 and 8 compare the present finite element solutions for u_θ and ω, respectively, with the corresponding analytical results, while the force tractions at A and B are provided in Table 2. All of the finite element solutions are in excellent agreement with the analytical solutions.

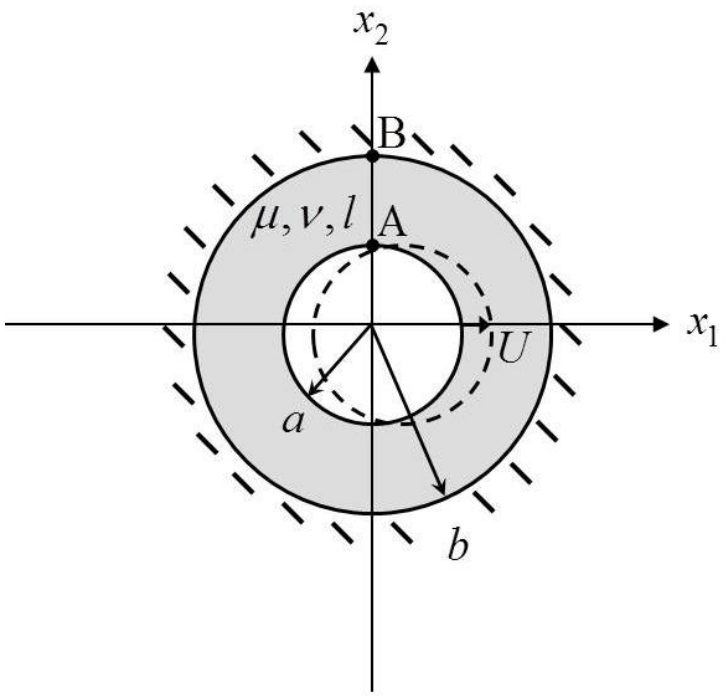

Fig. 6. Problem schematic of planar deformation of ring

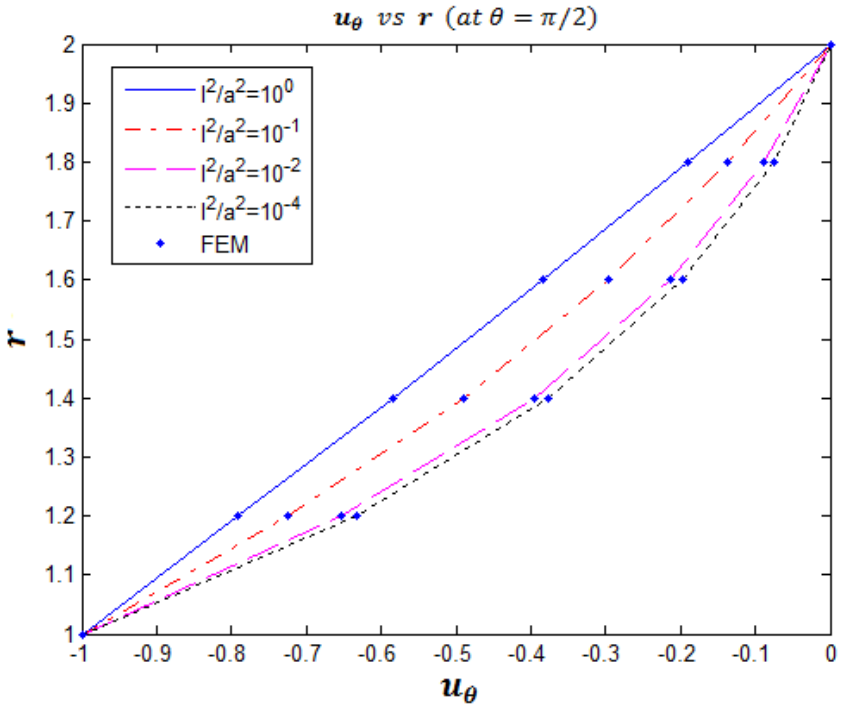

Fig. 7. Plot of u_θ for analytical and FEM solutions along center line $\theta = \pi/2$

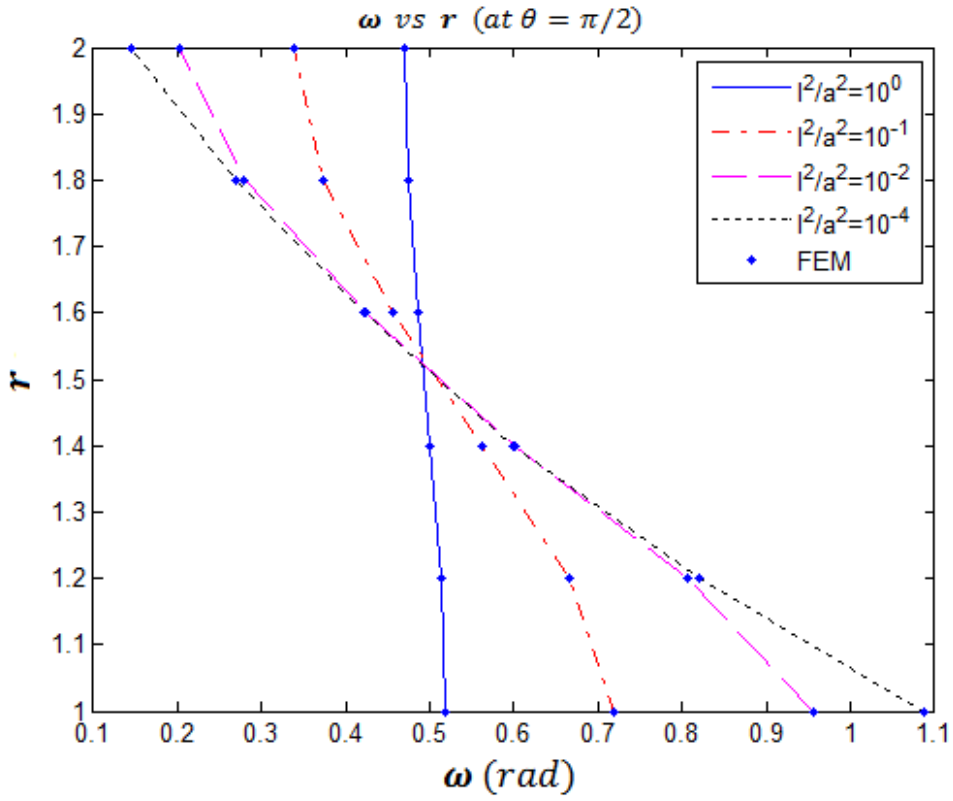

Fig. 8. Plot of ω for analytical and FEM solutions along center line $\theta = \pi/2$

Table 2. Results for tractions at points A and B

	$t_\theta(A)$			$t_\theta(B)$		
$\frac{l^2}{a^2}$	Analytical	FE	error	Analytical	FE	error
10^{-4}	-2.2096	-2.2095	4.53E-05	0.27614	0.27612	7.24E-05
10^{-2}	-2.2285	-2.2280	2.24E-04	0.2744	0.2744	1.82E-04
10^{-1}	-2.3310	-2.3312	8.58E-05	0.2880	0.2881	1.74E-04
10^{0}	-2.8192	-2.8255	2.23E-03	0.6682	0.6677	7.48E-04

2.4.3 *Transverse Plane-Strain Deformation of a Cantilever*

The final problem considered is the transverse deformation of a cantilever under plane strain conditions, including couple-stress effects. This problem, which has no existing analytical solution, is illustrated in Fig. 9. An enforced displacement in the vertical direction is applied to the right end of the cantilever. For material properties, we use $E = 2$ and $\nu = 0$ to provide a unit shear modulus and to allow for comparison with elementary theory for limiting values of the couple stress parameter l. The cantilever has height, h, which we consider to be the characteristic dimension for the problem. Meanwhile, for the length, we assume two different values; $L = 20h$ and $L = 40h$ to assure that under classical theory bending deformation will dominate for both aspect ratios.

Two sets of boundary conditions also are considered. For Case 1, the boundary conditions are as follows: on the left end zero displacement is enforced, while a unit vertical displacement is enforced on the right end. For Case 2, the rotations at the left end also are restrained to zero. In both cases, there are no applied force- and moment-tractions, and no applied body forces.

The mesh used here consists of rectangular elements arranged such that there are $20N$ elements lengthwise and $2N$ elements transversely. The finest mesh had $N = 8$ and therefore consisted of 2,560 elements. Figure 10 shows excellent convergence of the

total stored energy with uniform mesh refinement for Case 1 with $L = 20h$ and $h/l = 1$. For the remainder of these numerical experiments, the characteristic geometric length scale, h, is altered, while the material parameters are held constant. This is used to investigate the size-dependency inherent in the consistent couple-stress theory. Specifically, the stiffness of the beam, K, is of great interest, which is equal to the vertical right end displacement (at point A) divided by the vertical reaction force at that end. Figures 11a and b show the behavior of non-dimensional stiffness for Cases 1 and 2 of this length-scaling experiment. Meanwhile, Fig. 12 presents the deformed geometry of the cantilever with free rotations at the left end and $L = 20h$ for three distinct values of h/l.

From Figs. 11a and b, we can clearly see three well-defined domains associated with characteristic problem geometry. For large scale problems, where the characteristic geometry, h, is much greater than l, we have the classical elasticity region with stiffness independent of length scale. In this domain, couple-stress effects are negligible, mainly due to the small magnitude of curvature deformation at this scale. Notice that the stiffness is equal to $3EI/L^3$ in this region, as expected from classical beam theory.

When the characteristic geometry for this problem is on the order of l, we enter the transitional couple-stress domain. For this cantilever problem, it is clear from Figs. 11a and b that couple-stress effects become significant for characteristic geometry of

$h/l \approx 10$. In this couple-stress domain, there is an increase in flexural stiffness, which we see can have a significant effect on the overall effective stiffness of the body.

Finally, for very small values of h/l, we have a domain that is couple-stress "saturated" in both Figs. 11a and b. In other words, the flexural stiffness due to couple-stress effects has increased to the level where bending is suppressed, while shear deformation combined with rotation dominates. The absence of bending is clearly visible in the plot of deformed shape for $h/l = 0.0001$ in Fig. 12. Furthermore, from Fig. 11a, we find that for this particular problem, for sufficiently small h/l ratio, an increase in total stiffness by factors of 30 and 60 can be the result of including couple-stress effects with $L = 20h$ and $L = 40h$, respectively. In Case 2, where the rotational degree of freedom at the left hand end is set to zero in the couple stress formulation, an even more dramatic increase in stiffness is seen, corresponding very nearly to pure shear deformation of the beam. As a result, for this couple stress "saturated" domain in Case 2, we find $K \propto GA/L$. Meanwhile, for the corresponding domain in Case 1, the stiffness scales with $1/L^2$.

For the length scales defined in Figs. 11a and b, the saturated couple-stress region corresponds to a maximum possible stiffness for a given problem geometry and loading. Whether this totally saturated couple-stress region can occur in physical systems is undetermined at this point. Physical experimentation with the goal of testing for the couple-stress material property η or l is necessary to know exactly what portions of these couple-stress domains are physically realizable.

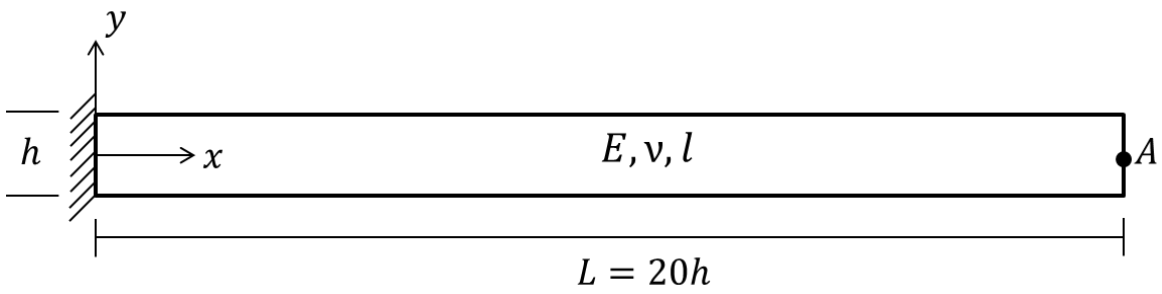

Fig. 9. Problem schematic of couple stress cantilever

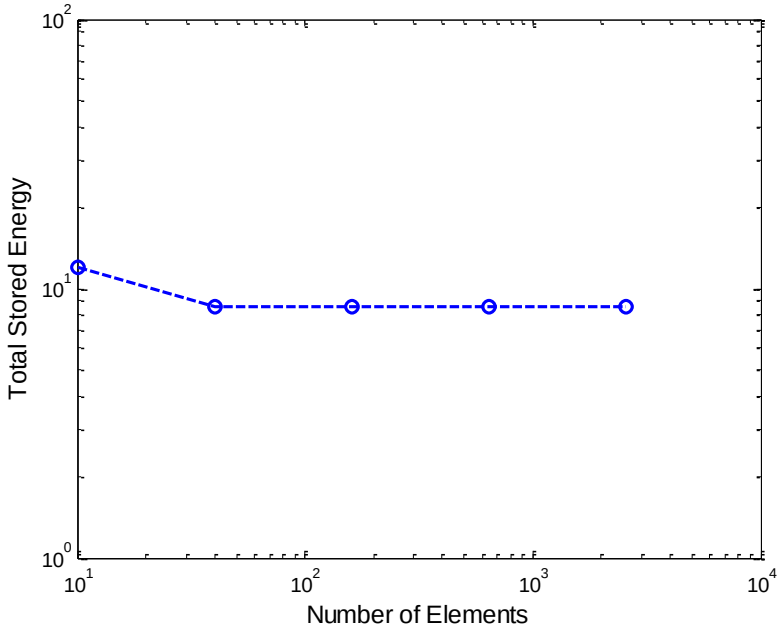

Fig. 10. Convergence of cantilever stored energy with mesh refinement

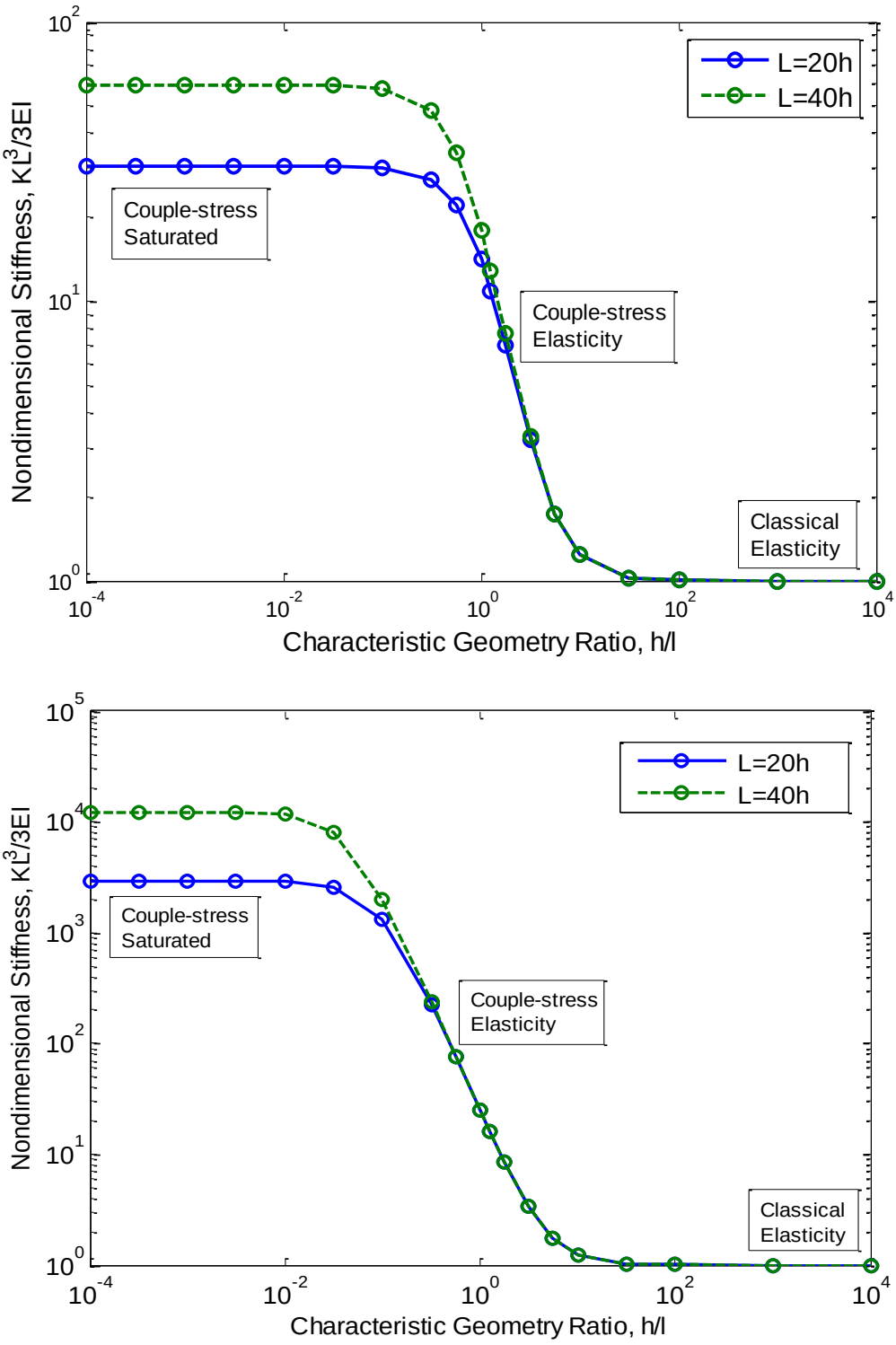

Fig. 11. Non-dimensional size-dependency of cantilever stiffness

(a) Case 1: $m = 0$ boundary condition at $x = 0$;
(b) Case 2: $\omega = 0$ boundary condition at $x = 0$.

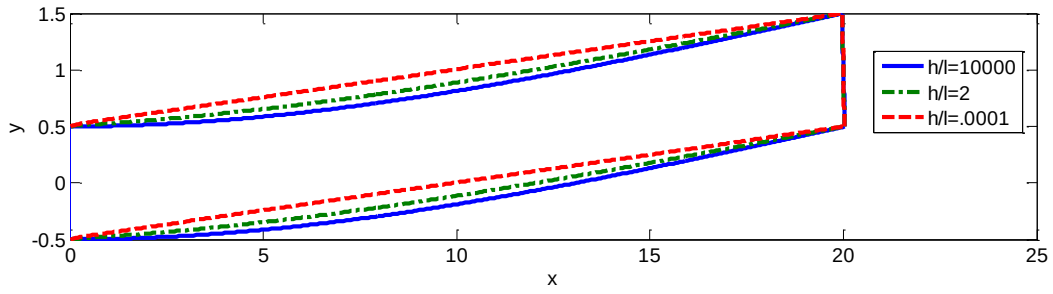

Fig. 12. Deformation of cantilever with $L = 20h$ and $m = 0$ boundary condition at $x = 0$ for select values of h/l

CHAPTER THREE

3 SIZE-DEPENDENT PIEZOELECTRICITY

3.1 Overview of Size-dependent Piezoelectric Theory

In this section, a brief overview of the important concepts and relations of consistent size-dependent piezoelectricity theory is provided, based on the work of Hadjesfandiari (2013). Particular attention is given to relations pertinent to the development of the finite element formulation presented in the next section. For a more detailed discussion on consistent size-dependent piezoelectricity, the reader is referred to Hadjesfandiari (2013).

At its simplest, linear size-dependent piezoelectricity can be described as the linear thermodynamic coupling between size-dependent elasticity and the electric polarization of a material. The theory presented here is based on the consistent skew-symmetric couple-stress theory (Hadjesfandiari and Dargush, 2011, 2013), which sets it apart from other size-dependent piezoelectricity and flexoelectricity theories. Furthermore, unlike the commonly accepted flexoelectric theory, the present formulation is consistent with Maxwell's equations of electromagnetism, which would seem to be a most important requirement. Details on the comparison can be found in Hadjesfandiari (2014). Because the present work is on size-dependent piezoelectricity as defined by Hadjesfandiari (2013), primary focus will be given to the extension of skew-symmetric couple-stress theory and not the fundamentals of the purely mechanical theory. For a detailed

description of skew-symmetric couple-stress theory, the reader is referred to Hadjesfandiari and Dargush (2011, 2013).

An overview of the underlying size-dependent elasticity formulation that the size-dependent piezoelectricity formulation presented in this section is based on is provided in chapter 2. From chapter 2, the elastic response of a two- or three-dimensional body under quasistatic loading is governed by equations (1) and (2), corresponding to linear and angular momentum balance, respectively. The natural boundary and essential boundary conditions for the elastic portion of the response remain governed by equations (3a-b) and (4a-b) from chapter 2. Finally, the relations between force-stress and force-traction, and couple-stress and moment-traction remain governed by equations (5a-b).

For a quasistatic electric field, E_i, we know that the curl vanishes. Because of this, we can relate the electric field to the gradient of a scalar electric potential φ, such that (Griffiths, 1989)

$$E_i = -\varphi_{,i} \tag{64}$$

In a piezoelectric material, an internal polarization field can be induced by deformation and the electric field. It is often convenient, however, to consider the electric displacement field, which is related to the electric field and polarization by

$$D_i = \varepsilon_o E_i + P_i \tag{65}$$

where D_i is the electric displacement vector and P_i is the polarization. For linear dielectric materials, the polarization can be related to the electric field in a linear fashion, and hence so can the electric displacement.

The normal component of the electric displacement, $\mathcal{d}$, on the surface is related to D_i by

$$\mathcal{d} = D_i n_i \tag{66}$$

The governing differential equation for the electric displacement in a dielectric body is the Gauss law in differential form, given by

$$D_{i,i} = \bar{\rho}_E \tag{67}$$

where $\bar{\rho}_E$ is an applied body charge density. Note that this is a scalar quantity and the subscript is merely meant to distinguish the body charge density from the mass density.

At the interface between two different materials, the normal electric displacement is related to the free surface charge, q_s, by

$$q_s = \lfloor \mathcal{d} \rfloor \tag{68}$$

where $\lfloor \cdot \rfloor$ denotes the jump across the interface. It is common in other works to specify free surface charge for the natural boundary conditions related to the electric displacement. However, this is only valid when the external electric displacement is negligible. More generally, the natural boundary conditions can be specified in terms of

d, which is what will be used here. Then, for natural and essential boundary conditions, respectively, we have the following:

$$d = \bar{d} \quad \text{on} \quad S_d \tag{69}$$

and

$$\varphi = \bar{\varphi} \quad \text{on} \quad S_\varphi \tag{70}$$

For a well-defined boundary value problem, we should have $S_d \cup S_\varphi = S$, and $S_d \cap S_\varphi = \emptyset$.

From Hadjesfandiari (2013), the electromechanical enthalpy density, H, of a linear, centrosymmetric material can be expressed as

$$H = \frac{1}{2} e_{ij} c_{ijkl} e_{kl} + \frac{1}{2} k_i b_{ij} k_j - \frac{1}{2} E_i \varepsilon_{ij} E_j - E_i \gamma_{ij} k_j \tag{71}$$

where c_{ijkl} is the standard 4th order constitutive tensor used for classical linear elasticity theories. In the isotropic case, the response depends on two elastic coefficients, for example, the Lamé constants λ and G. For cubic materials with centrosymmetry, there are three independent elastic coefficients c_{1111}, c_{1122}, and c_{1212} which in Voigt notation are written instead as c_{11}, c_{12} and c_{44}, respectively. More detail can be found in Hadjesfandiari (2014).

In addition, b_{ij} is the 2nd order linear couple-stress-curvature constitutive tensor, ε_{ij} is the total electric permittivity tensor and γ_{ij} is the coupling tensor for the electric field and curvature. The presence of this coupling term in the electric enthalpy is what allows for piezoelectric effects within a centrosymmetric body. For isotropic and centrosymmetric cubic materials, this piezoelectric-curvature coupling tensor can be written in terms of a single piezoelectric-curvature parameter, $\breve{f}$, as

$$\gamma_{ij} = 2\,\breve{f}\,\delta_{ij} \tag{72}$$

The piezoelectric-curvature parameter used in this thesis is related to the parameter, f, defined in Hadjesfandiari (2013), such that

$$\breve{f} = -f \tag{73}$$

This sign change of $\breve{f}$ relative to f is a consequence of the choice of curvature vector that is used in the present thesis. By using this definition of the piezoelectric-curvature parameter, we have that for materials with positive $\breve{f}$, an electric field directed in the positive direction will induce positive ("concave upwards") curvature deformation and vice versa. The electric enthalpy density of course remains unchanged by this choice of parameter.

The total electric permittivity tensor is

$$\varepsilon_{ij} = \varepsilon_r \varepsilon_0 \delta_{ij} \tag{74}$$

where ε_0 is the electric permittivity in a vacuum and ε_r is the relative electric permittivity. The couple-stress constitutive tensor for centrosymmetric cubic and isotropic materials is written previously in (22).

More generally, H could also include coupling between strain and curvature, and of course strain and electric field, such as for classical piezoelectricity, however these coupled effects do not exist in the centrosymmetric dielectric materials considered here. Also, it is equally valid to write H in terms of the mean curvature tensor; however from now on we will use the engineering mean curvature vector for simplicity.

The electromechanical enthalpy density is related to the positive definite internal energy density, U, by

$$H = U - E_i D_i \tag{75}$$

Hadjesfandiari (2013) derives the constitutive equations for the symmetric stress, electric displacement, and couple-stress from H as follows:

$$\sigma_{(ji)} = \frac{\partial H}{\partial e_{ij}} = c_{ijkl} e_{kl} \tag{76a}$$

$$\mu_i = \frac{\partial H}{\partial k_i} = b_{ij} k_j - \gamma_{ji} E_j \tag{77a}$$

$$D_i = -\frac{\partial H}{\partial E_i} = \varepsilon_{ij} E_j + \gamma_{ij} k_j \tag{78a}$$

For an isotropic material, these reduce to (Hadjesfandiari, 2013)

$$\sigma_{(ji)} = \lambda e_{kk}\delta_{ij} + 2Ge_{ij} \tag{76b}$$

$$\mu_i = 4Gl^2 k_i - 2\check{f}E_i \tag{77b}$$

$$D_i = \varepsilon E_i + 2\check{f}k_i \tag{78b}$$

while for centrosymmetric cubic material, the corresponding relations are given in Hadjesfandiari (2014).

3.2 Size-dependent Piezoelectric Variational Formulation

The total electromechanical enthalpy of the system Π_H is defined in Hadjesfandiari (2013) as

$$\Pi_H = \int_V H\, dV + \mathcal{W} \tag{79}$$

where $\mathcal{W}$ is the total potential from applied forces, moments, and normal electric displacement given by

$$\mathcal{W} = -\int_V u_i \overline{F_i}\, dV + \int_V \varphi \bar{\rho}_E\, dV - \int_{S_t} u_i \bar{t}_i\, dS - \int_{S_m} \omega_i \overline{m}_i\, dS - \int_{S_d} \varphi \bar{d}\, dS \tag{80}$$

Therefore, for the total electromechanical enthalpy Π_H, we have

$$\Pi_H = \frac{1}{2}\int_V e_{ij}c_{ijlm}e_{lm}\,dV + \frac{1}{2}\int_V k_i b_{ij} k_j\,dV - \frac{1}{2}\int_V E_i \varepsilon_{ij} E_j\,dV - \int_V E_i \gamma_{ij} k_j\,dV$$
$$- \int_V u_i \bar{F}_i\,dV + \int_V \varphi \bar{\rho}_E\,dV - \int_{S_t} u_i \bar{t}_i\,dS - \int_{S_m} \omega_i \bar{m}_i\,dS \tag{81}$$
$$- \int_{S_d} \varphi \bar{d}\,dS$$

By substituting the kinematic relations, this total electromechanical enthalpy can of course be written as a function of only displacement and electric potential

$$\Pi_H \equiv \Pi_H(e(u), k(u), u, E(\varphi)) \tag{82}$$

Now this functional may be extremized by taking the first variation and setting it equal to zero. This however leads to a formulation that requires C^1 continuity of the displacement field.

A better approach, as shown for the purely mechanical problem in section 2.2 of the present work, is to consider independent displacements and rotations and then enforce the rotation-displacement compatibility constraint of (7b) by including Lagrange multipliers into the enthalpy functional prior to extremizing. Thus, we define a new functional

$$\Pi_H^* \equiv \Pi_H^*(e(u), k(\omega), u, \omega, E(\varphi), \lambda) \tag{83}$$

where

$$\Pi_H^* = \Pi_H + \int_V \lambda_k \left(\varepsilon_{kji} u_{i,j} - 2\omega_k\right) dV \tag{84}$$

It is shown in section 2.2 that by extremizing the functional for the mechanical problem that these Lagrange multipliers turn out to be equal to the skew-symmetric stress vector, s_i. This is an extremely convenient property of the variational formulation, because otherwise the skew-symmetric part of the stress tensor would be difficult to obtain. The same feature carries over to the couple stress piezoelectric variational principle presented here.

We then have the following C^0 variational problem

$$\delta\Pi_H^* = \frac{\partial\Pi_H^*}{\partial u_i}\delta u_i + \frac{\partial\Pi_H^*}{\partial \omega_i}\delta\omega_i + \frac{\partial\Pi_H^*}{\partial\varphi}\delta\varphi + \frac{\partial\Pi_H^*}{\partial s_i}\delta s_i = 0 \tag{85}$$

where

$$\Pi_H^* = \Pi_H^*(e(u), k(\omega), u, \omega, E(\varphi), s) = \Pi_H + \int_V s_k\left(\varepsilon_{ijk}u_{j,i} - 2\omega_k\right) dV \tag{86}$$

In section 2.2 it is shown by deriving the corresponding Euler-Lagrange equations that the solutions to the variational problem of (85) satisfy linear and angular momentum balances, rotation-displacement compatibility, and force and moment traction boundary conditions. Following the same derivations as in section 2.2, it is a simple task to show that evaluating the third term of (85) will also produce Euler-Lagrange equations corresponding to Gauss' law in differential form, (67), and the natural boundary conditions corresponding to (69).

Before developing the corresponding finite element formulation in the next section, we should emphasize the differences first developed in Hadjesfandiari (2014) between the present size-dependent piezoelectric theory and the prevailing flexoelectric version. In particular, the present theory is consistent with Maxwell's equations of electromagnetism and the self-consistent theory of couple stresses, while the latter satisfies neither of these essential conditions. Furthermore, the present theory predicts that only two additional parameters, l and $\check{f}$, appear for isotropic or centrosymmetric cubic materials, rather than three as required for the predominant flexoelectric theory. In this regard, we point to the difficulties expressed by Zubko et al. (2007) in estimating these three material parameters for cubic $SrTiO_3$ single crystals. Several statements in Zubko et al., (2007) suggest that perhaps the three flexoelectric material parameters are not independent. Two recent reviews on flexoelectricity express further concerns relating to the prevailing theory (Zubko et al., 2013; Yudin and Tagantsev, 2013). Thus, further physical and computational experiments are needed to clarify the underlying theory. The finite element formulation to be developed in the following section can be quite useful for those investigations.

3.3 Size-dependent Piezoelectric Finite Element Formulation

As with most continuum theories, the analytical solutions that are available are limited to very simple geometry and boundary conditions. Clearly numerical formulations must be developed in order to analyze real world problems that arise in the design process of modern technologies looking to take advantage of size-dependent piezoelectric effects. In this section a finite element formulation is developed for linear, centrosymmetric cubic and isotropic, piezoelectric solids based on the size-dependent theory of Hadjesfandiari (2013, 2014).

Voigt notation is used in this section for the purpose of simplifying calculations and programming. This means that the strain, $\boldsymbol{e}$, is represented by a vector rather than a second order tensor, and the constitutive tensor, $\boldsymbol{c}$, is expressed as a two-dimensional matrix rather than a fourth order tensor. For the two-dimensional, plane-strain, linear problems that we will explore here, we then have the following representations:

$$\boldsymbol{e} = \begin{bmatrix} e_{xx} \\ e_{yy} \\ \gamma_{xy} \end{bmatrix} = \begin{bmatrix} \frac{\partial u_x}{\partial x} \\ \frac{\partial u_y}{\partial y} \\ \frac{\partial u_x}{\partial y} + \frac{\partial u_y}{\partial x} \end{bmatrix} \tag{87}$$

$$\boldsymbol{c} = \begin{bmatrix} c_{11} & c_{12} & 0 \\ c_{12} & c_{11} & 0 \\ 0 & 0 & c_{44} \end{bmatrix} \tag{88a}$$

which specializes as follows for the isotropic case

$$\boldsymbol{c} = \frac{E(1-\nu)}{(1+\nu)(1-2\nu)} \begin{bmatrix} 1 & \frac{\nu}{1-\nu} & 0 \\ \frac{\nu}{1-\nu} & 1 & 0 \\ 0 & 0 & \frac{1-2\nu}{2(1-\nu)} \end{bmatrix} \tag{88b}$$

Here u_x is the component of displacement in the x-direction and u_y is the component of the displacement in the y-direction. Additionally, E is the Young's modulus, and ν is the Poisson's ratio. For plane-stress problems, only the matrix $\boldsymbol{c}$ will need to change (Bathe, 1996).

For planar problems, the engineering mean curvature vector can be written in terms of the one out of plane component of rotation, ω, explicitly as

$$\boldsymbol{k} = \begin{bmatrix} k_x \\ k_y \end{bmatrix} = \begin{bmatrix} -\frac{\partial \omega}{\partial y} \\ \frac{\partial \omega}{\partial x} \end{bmatrix} \tag{89}$$

The couple-stress constitutive matrix for linear centrosymmetric cubic and isotropic materials is represented by (46), while the corresponding piezoelectric-curvature coupling tensor, $\boldsymbol{\gamma}$, becomes

$$\boldsymbol{\gamma} = 2\,\check{f} \begin{bmatrix} 1 & 0 \\ 0 & 1 \end{bmatrix} \tag{90}$$

From (64), we can express the electric field in terms of the electric potential as

$$\boldsymbol{E} = \begin{bmatrix} E_x \\ E_y \end{bmatrix} = \begin{bmatrix} -\frac{\partial \varphi}{\partial x} \\ -\frac{\partial \varphi}{\partial y} \end{bmatrix} \tag{91}$$

We now consider the variational principle posed in the previous section. In vector notation, we have

$$\delta \Pi_H^* = 0 = \frac{\partial \Pi_H^*}{\partial \boldsymbol{u}} \delta \boldsymbol{u} + \frac{\partial \Pi_H^*}{\partial \boldsymbol{\omega}} \delta \boldsymbol{\omega} + \frac{\partial \Pi_H^*}{\partial \varphi} \delta \varphi + \frac{\partial \Pi_H^*}{\partial \boldsymbol{s}} \delta \boldsymbol{s} \tag{92}$$

where

$$\begin{aligned} \Pi_H^* = \frac{1}{2}\int_V \boldsymbol{e}^T \boldsymbol{c}\boldsymbol{e}\, dV + \frac{1}{2}\int_V \boldsymbol{k}^T \boldsymbol{b}\boldsymbol{k}\, dV + \int_V (curl\, \boldsymbol{u} - 2\boldsymbol{\omega})^T\, \boldsymbol{s}\, dV - \frac{1}{2}\int_V \boldsymbol{E}^T \boldsymbol{\varepsilon}\boldsymbol{E}\, dV \\ - \int_V \boldsymbol{E}^T \boldsymbol{\gamma}\boldsymbol{k}\, dV - \int_V \boldsymbol{u}^T \overline{\boldsymbol{F}}\, dV + \int_V \varphi \bar{\rho}_E\, dV - \int_{S_t} \boldsymbol{u}^T \bar{\boldsymbol{t}}\, dS \\ - \int_{S_m} \boldsymbol{\omega}^T \overline{\boldsymbol{m}}\, dS - \int_{S_d} \varphi \bar{d}\, dS \end{aligned} \tag{93}$$

Next, following section 2.3, the domain is divided into finite elements. Figure 13 shows the 8-node isoparametric quadrilateral master element used in the present formulation. This element has natural coordinates represented by r and s, with values for each element ranging from -1 to +1 in either direction. In the global coordinate system, here represented in two dimensions by normal Cartesian coordinates x and y, our element can take on any arbitrary shape, limited only by the need to maintain a well-defined Jacobian (Bathe, 1996; Zienkiewicz and Taylor, 2000).

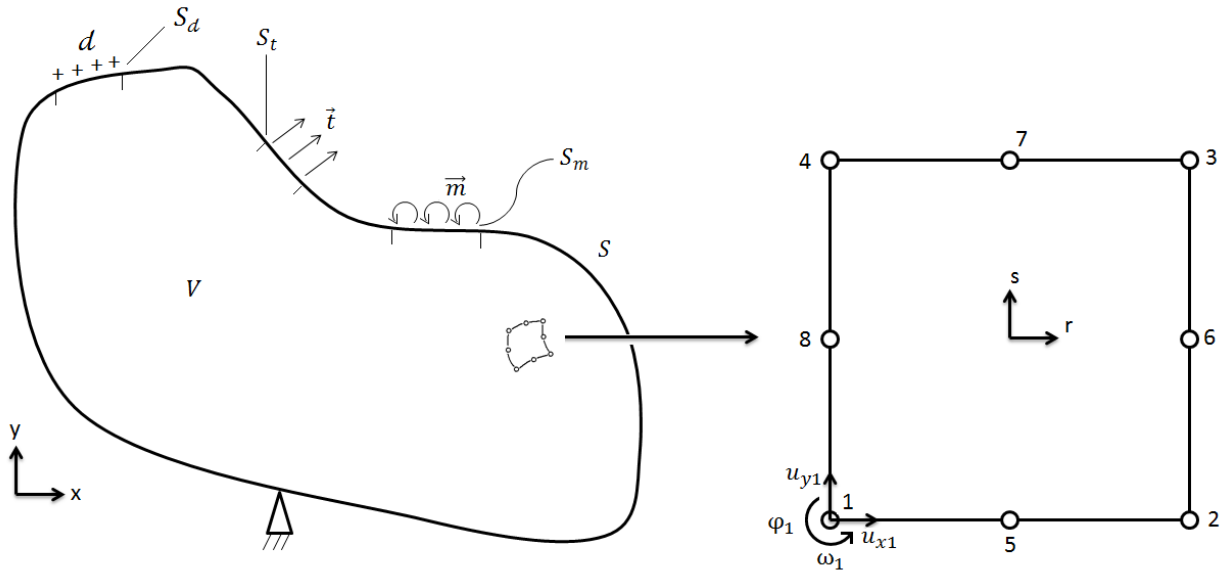

Fig. 13. General planar body and 8-node master element

The same quadratic shape functions $\boldsymbol{N}$, that were used in section 2.3 (Zienkiewicz and Taylor, 2000; Bathe, 1996) are used in this formulation. These shape function are given explicitly by (49).

These shape functions, $\boldsymbol{N}$, are used to interpolate both the geometric coordinates of the element as well as the displacement and rotation within an element as shown by (50) and (51). Additionally, these shape function are now used to interpolate electric potential within an element, such that

$$\varphi \cong \boldsymbol{N}\hat{\boldsymbol{\varphi}} \tag{94}$$

recalling that the hat represent a vector with nodal quantities ranging from 1 to 8.

Similarly, the displacements, rotations, and electric potential on the boundaries S_t, S_m, and S_d are interpolated using the surface shape functions, $\boldsymbol{N_S}$, given by (53). Then for the interpolation of electric potential on an element surface we have

$$\varphi_{S_d} \cong \boldsymbol{N_S}\widehat{\boldsymbol{\varphi}} \tag{95}$$

The interpolated approximations for strain and curvature are given previously by (54) and (55). Now, the electric field in (48) can be replaced by the following discrete approximation

$$\boldsymbol{E} \cong \boldsymbol{B_E}\widehat{\boldsymbol{\varphi}} \tag{96}$$

where $\boldsymbol{B_E}$ is the electric field-potential matrix and can be written explicitly as

$$\boldsymbol{B_E} = \begin{bmatrix} -\frac{\partial N_1}{\partial x} & -\frac{\partial N_2}{\partial x} & \cdots & -\frac{\partial N_7}{\partial x} & -\frac{\partial N_8}{\partial x} \\ -\frac{\partial N_1}{\partial y} & -\frac{\partial N_2}{\partial y} & & -\frac{\partial N_7}{\partial y} & -\frac{\partial N_8}{\partial y} \end{bmatrix} \tag{97}$$

The other $\boldsymbol{B}$ matrices are shown explicitly in (57a-c). For all cases, the $\boldsymbol{B}$ matrices are functions of the first derivatives of the shape functions with respect to global Cartesian coordinates, x and y.

For 2-d problems the skew-symmetric stress pseudo vector simplifies to one component in the out-of-plane direction. Further simplifying matters, we need only C^{-1} continuity in this formulation and therefore consider $\boldsymbol{s}$ to be constant throughout each element.

Now, upon substitution of the discrete representations of our variables into (93), and then taking the first variation with respect to the discrete variables, we are left with the following for each element

$$\begin{aligned}\delta\Pi_H^* = 0 = (\delta\hat{\boldsymbol{u}})^T & \left[\int_V (\boldsymbol{B}^T \boldsymbol{c}\boldsymbol{B})\,\hat{\boldsymbol{u}}\, J_d dV + \int_V \boldsymbol{B_{curl}}^T \boldsymbol{s}\, J_d\, dV - \int_V \boldsymbol{N}^T \bar{\boldsymbol{F}}\, J_d dV - \int_{S_t} \boldsymbol{N}_S^T \bar{\boldsymbol{t}}\, J_{dS}\, dS\right] \\ & + (\delta\hat{\boldsymbol{\omega}})^T \left[\int_V (\boldsymbol{B}_{\boldsymbol{k}}^T \boldsymbol{b}\boldsymbol{B}_{\boldsymbol{k}})\,\hat{\boldsymbol{\omega}}\, J_d dV - \int_V (\boldsymbol{B}_{\boldsymbol{k}}^T \boldsymbol{\gamma}\boldsymbol{B}_{\boldsymbol{E}})\,\hat{\boldsymbol{\varphi}}\, J_d dV\right. \\ & \left. + \int_V -2\boldsymbol{N}^T \boldsymbol{s}\, J_d dV - \int_{S_m} \boldsymbol{N}_S^T\, \bar{\boldsymbol{m}}\, J_{dS}\, dS\right] + (\delta \boldsymbol{s}) \left[\int_V (\boldsymbol{B_{curl}}\hat{\boldsymbol{u}} - 2\boldsymbol{N}\hat{\boldsymbol{\omega}})\, J_d dV\right] \\ & + (\delta\hat{\boldsymbol{\varphi}})^T \left[-\int_V (\boldsymbol{B}_{\boldsymbol{E}}^T \boldsymbol{\varepsilon}\boldsymbol{B}_{\boldsymbol{E}})\,\hat{\boldsymbol{\varphi}}\, J_d dV - \int_V (\boldsymbol{B}_{\boldsymbol{E}}^T \boldsymbol{\gamma}\boldsymbol{B}_{\boldsymbol{k}})\,\hat{\boldsymbol{\omega}}\, J_d dV + \int_V \boldsymbol{N}^T \bar{\rho}_E\, dV\right. \\ & \left. - \int_{S_\sigma} \boldsymbol{N}_S^T\, \bar{d}\, dS\right]\end{aligned} \tag{98}$$

where J_d and J_{dS} represent the determinants of the Jacobian of the volume and the surface of an element, respectively. For the integration over the 8-noded isoparametric size-dependent piezoelectric elements presented here, standard 3×3 point Gauss quadrature is used (Bathe, 1996; Zienkiewicz and Taylor, 2000).

Due to the fact that the variational factors, $\delta\hat{\boldsymbol{u}}$, $\delta\hat{\boldsymbol{\omega}}$, $\delta\hat{\boldsymbol{\varphi}}$, and $\delta\boldsymbol{s}$ have arbitrary value, the four terms in square brackets above all must be identically zero for this equation to be valid. This provides us with four coupled sets of linear algebraic equations for each element. These are our final finite element equations for a single element in matrix form.

We now have a set of linear algebraic equations for each element. Here we choose to organize these element equations into the form shown in Fig. 14.

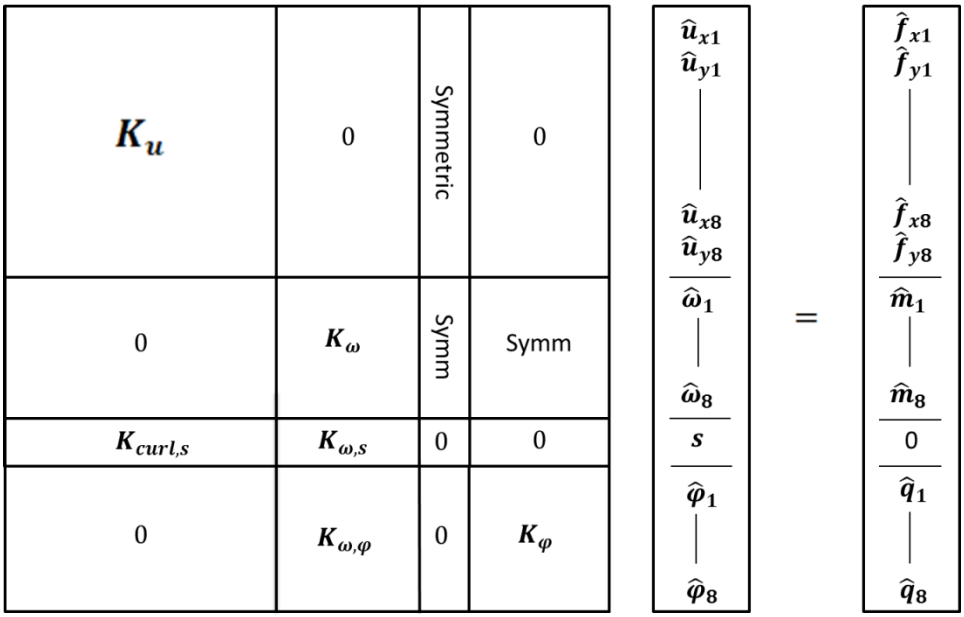

Fig. 14. Structure of resulting element equations before assembly

Corresponding to (98), the stiffness terms on the left hand side are calculated explicitly as follows:

$$\boldsymbol{K_u} = \int_V (\boldsymbol{B}^T \boldsymbol{C} \boldsymbol{B})\, J_d dV \tag{99a}$$

$$\boldsymbol{K_\omega} = \int_V (\boldsymbol{B_k^T b B_k})\, J_d dV \tag{99b}$$

$$\boldsymbol{K_{curl,s}} = \int_V (\boldsymbol{B_{curl}})\, J_d dV \tag{99c}$$

$$\boldsymbol{K_{\omega,s}} = -\int_V (2\boldsymbol{N})\, J_d dV \tag{99d}$$

$$\boldsymbol{K_{\omega,\varphi}} = -\int_V (\boldsymbol{B_E^T \gamma B_k})\, J_d dV \tag{99e}$$

$$\boldsymbol{K_\varphi} = -\int_V (\boldsymbol{B_E^T \varepsilon B_E})\, J_d dV \tag{99f}$$

Meanwhile, for the right hand side, we have

$$\hat{\boldsymbol{f}}_{\boldsymbol{x}} = \int_V \boldsymbol{N}^T \bar{F}_x \, J_d dV + \int_{S_t} \boldsymbol{N}_S^T \, \bar{t}_x \, J_{dS} \, dS \tag{100a}$$

$$\hat{\boldsymbol{f}}_{\boldsymbol{y}} = \int_V \boldsymbol{N}^T \bar{F}_y \, J_d dV + \int_{S_t} \boldsymbol{N}_S^T \, \bar{t}_y \, J_{dS} \, dS \tag{100b}$$

$$\hat{\boldsymbol{m}} = \int_{S_m} \boldsymbol{N}_S^T \, \bar{m} \, J_{dS} \, dS \tag{100c}$$

$$\hat{\boldsymbol{q}} = -\int_V \boldsymbol{N}^T \bar{\rho}_E \, J_d dV + \int_{S_d} \boldsymbol{N}_S^T \, \bar{d} \, J_{dS} dS \tag{100d}$$

where the subscripts x and y above indicate the components of force in that respective direction. All terms that appear in the right hand side are of course known quantities, as indicated by the overbars in (100a-d).

After evaluating the stiffness matrix and forcing vector on the element level, we then follow standard finite element procedures (Bathe, 1996; Zienkiewicz and Taylor, 2000) to assemble and solve the global set of linear algebraic equations

$$\boldsymbol{K}\boldsymbol{u} = \boldsymbol{f} \tag{101}$$

where now $\boldsymbol{u}$ includes all nodal values for displacement, rotation, and electric potential, along with the element-based skew-symmetric stress.

Before considering the solution to several boundary value problems, two additional points should be made. The first relates to the introduction of the skew-symmetric stress Lagrange multipliers to enforce the displacement-rotation constraint. Notice that the

corresponding diagonal block of the stiffness matrix displayed in Fig. 14 becomes zero and, as a consequence, the overall system matrix in (101) is indefinite. Consequently, sophisticated direct solvers appropriate for sparse, symmetric, indefinite matrices are needed to maintain accuracy of the solution. In the present work, the MATLAB (2014) implementation of the unsymmetric multifrontal sparse LU factorization package UMFPACK is used with a symmetric pivoting strategy (Davis and Duff, 1997; Davis, 2004).

The second point relates to Dirichlet boundary conditions that must be enforced on surfaces with fixed non-zero displacement, rotation, and/or electric potential. There are many ways to do this. One simple approach is to replace the corresponding right hand side component with the specified boundary value and then multiply both the corresponding diagonal and right hand side components by a sufficiently large penalty parameter. However, due to the sensitive nature of the indefinite system equations associated with the present formulation, we prefer to avoid penalty parameters. Instead, we modify the right hand side by subtracting the product of the columns corresponding to the specified nodal degrees of freedom and the enforced boundary value. Then, the corresponding rows and columns can be zeroed, while the diagonal value is set to unity and the corresponding right hand side entry is equated to the desired value of displacement, rotation, or electric potential.

3.4 Size-dependent Piezoelectric Problems

3.4.1 *Isotropic cylinder with constant applied electric field on surface*

For this problem we consider a long, isotropic, circular cylinder with radius a. The surface of the cylinder is exposed to an applied constant electric field of magnitude E_0 directed in the positive x-direction. This serves as a direct Dirichlet boundary condition on the electric potential. Clearly from (64) the boundary condition for electric potential will be

$$\varphi = -E_0 a \cos\theta \tag{102}$$

on surface $r = a$.

The other boundary conditions for this problem are zero force- and moment-tractions on the surface, along with constrained displacement and rotation of the center point. The problem geometry may also be simplified by enforcing certain symmetry boundary conditions along the horizontal and vertical axes. Specifically, the boundary conditions for the vertical axis are zero electric potential, zero vertical displacement, zero horizontal force-traction, and zero moment-traction. The boundary conditions for the horizontal axis are zero normal electric displacement, zero vertical displacement, zero horizontal force-traction, and zero moment-traction. By enforcing these boundary conditions only the first quadrant of the cylinder geometry needs to be considered.

For material properties in dimensionless form we consider $E = 5/2$, $\nu = 1/4$, and $\varepsilon = 1$. The magnitude of the applied electric field is considered unity for all simulations here. An unstructured mesh with 126 elements is used.

The problem has an analytical solution derived in Hadjesfandiari (2013) that will be used to validate the numerical solutions here. Displacement results are presented in Table 3, where U_0 is the horizontal displacement at the point on the surface at $\theta = 0$, and U_{90} is the horizontal displacement at the point on the surface at $\theta = \pi/2$. From Table 3, we see that the numerical solutions are in excellent agreement with the analytical solution.

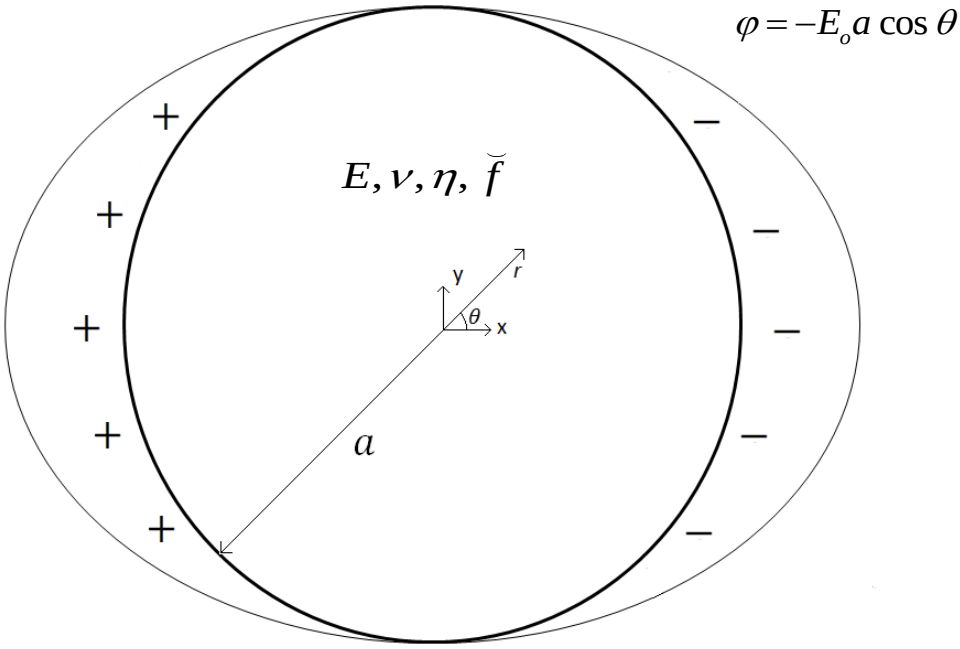

Fig. 15. Problem schematic of long cylinder with constrained potential on surface

Table 3. Results for long cylinder with constant applied electric field on surface

$\check{f}$	η	Analytical (Hadjesfandiari, 2013)		FE (126 elements)		Relative Error: $\frac{U_{FE}-U_{analytic}}{U_{analytic}}$	
		U_{90}	U_0	U_{90}	U_0	U_{90}	U_0
0	0.1	0	0	0	0	0	0
0.01	0.1	0.0156683	0.0016525	0.0156677	0.0016488	-3.63E-05	-2.21E-03
0.1	0.1	0.1566826	0.0165248	0.1566769	0.0164883	-3.63E-05	-2.21E-03
1	0.1	1.5668259	0.1652484	1.5667691	0.1648831	-3.63E-05	-2.21E-03
0.1	0.01	0.2647973	0.0099273	0.2642131	0.0096449	-2.21E-03	-2.84E-02
0.1	1	0.0311736	0.0042998	0.0311788	0.0042982	1.68E-04	-3.74E-04

3.4.2 *Slender isotropic cantilever in constant transverse electric field (normalized paramters)*

Here we consider a long, isotropic cantilever with a constant electric potential applied to the top and bottom surfaces. The upper surface can be considered grounded with $\varphi = 0$ and the bottom surface is held at a value of $\varphi = h$. Note that again we are considering all quantities to be dimensionless here. These conditions on the potential will produce a unit uniform constant electric field in the positive y- direction, which in turn induces curvature in the beam. This problem is useful for exploring both the direct connection between electric field and curvature present in consistent couple stress piezoelectricity, and the size-dependency of the electromechanical phenomena. This problem also has

significance to the development of small scale sensors and actuators. From the above problem definition, the vertical electric field can be calculated by

$$E_y \cong \frac{\varphi_{bottom}-\varphi_{top}}{h} = \frac{\Delta\varphi}{h} = 1 \tag{103}$$

The material parameters in non-dimensional form for this beam are as follows: $E = 2$, $l = 1$, $\check{f} = 1$, $\varepsilon = 1$ and $\nu = 0$. Aside from the electric potential boundary condition specified on the top and bottom surface, the following boundary conditions are enforced; there is no applied force- or moment-tractions, the left and right hand sides are considered to be electrically insulated such that $\mathcal{d} = 0$, and finally the vertical displacements, horizontal displacements, and the rotations on the surface with $x = 0$ are constrained to be zero.

The mesh used here consists of rectangular elements arranged such that there are $20N$ elements lengthwise and $2N$ elements transversely. The finest mesh had $N = 8$ and therefore consisted of 2,560 elements. Figure 17 shows excellent convergence of the vertical end displacement, U_y, with uniform mesh refinement for the case with $h/l = 1$. For the numerical experiments with results presented in Figs. 18 and 19, the characteristic geometry, h, was varied in order to show the size-dependency of the theory.

For a long slender beam, such as the one examined here, we expect the assumptions of an Euler-Bernoulli beam model to hold true. Recently, an Euler-Bernoulli beam model based on the consistent size-dependent piezoelectric theory presented in Hadjesfandiari

(2013) was derived in Li et al. (2014). From this paper the vertical displacements of the beam should be:

$$u_y(x) \approx \frac{b\check{f}\Delta\varphi}{\frac{EI}{2} + 2Gl^2A} x^2 \tag{104}$$

where b is the beam depth, I is the area moment of inertia, and A is the cross sectional area. This solution corresponds to constant curvature in the y-direction. The induced curvature however is clearly size-dependent. For small scales ($h/l < 1$) we expect the term involving the couple-stress parameter to limit the induced curvature such that:

$$k_y \approx \frac{b\check{f}\Delta\varphi}{2Gl^2A} = \frac{\check{f}E_y}{2Gl^2} \tag{105}$$

For larger scales ($h/l \gg 1$), we expect the classical bending stiffness term to limit the induced curvature such that:

$$k_y \approx \frac{b\check{f}\Delta\varphi}{EI/2} = \frac{24\check{f}E_y}{Eh^2} \tag{106}$$

The results using the FE formulation developed here show that indeed the solution to this problem is a field with constant k_y, with the exception of minor edge effects at the right boundary. The solutions are in excellent agreement with equations (104) through (106). From Fig. 18, we see that for very small characteristic geometry ($h/l < 1$) we have for the induced curvature, $k_y = \check{f}\, E_y/2Gl^2$. For increasing characteristic geometry starting from $h/l \approx 10$, we note that k_y decreases proportional to $1/h^2$, as expected from (106). This size-dependent behavior leads to some maximum end displacement that is possible for this size-dependent piezoelectric problem. This is very interesting because it means

that even for very large geometries we will still have some displacement that is not dependent on the cantilever geometry. In other words even for large scales the size-dependent piezoelectric effect is non-zero. However, as one can see from Fig. 19, the ratio of the vertical end displacement at point A to the cantilever geometry, U_y/L, is decreasing proportional to $1/h$. Then, for larger length scales, we can conclude that the deformation due to the size-dependent piezoelectric effect, although equal to some nonzero value, will become negligible and perhaps even impossible to detect. Also from Fig. 19, we see that the size-dependent piezoelectric effects relative to size of the cantilever are greatest for $h/l \approx 5$. We should note that generally results will deviate from (104) for real materials due to non-zero Poisson's ratio. The formulation developed here is capable of accurately modeling this effect too.

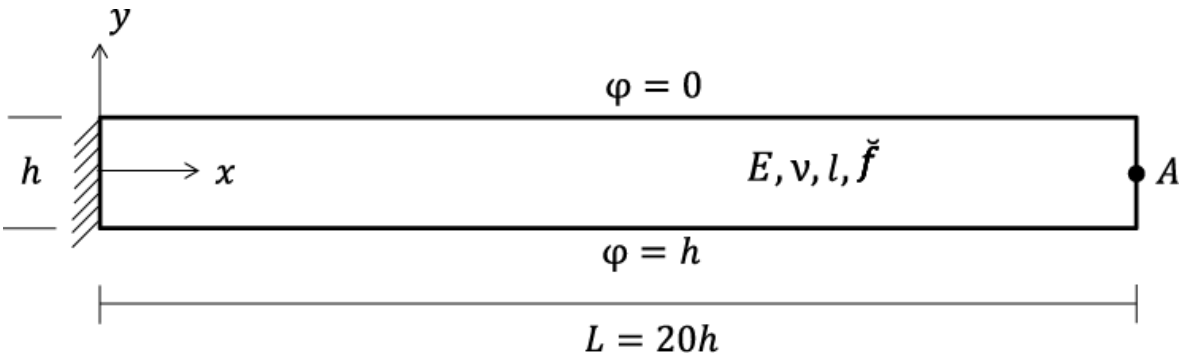

Fig. 16. Problem schematic of size-dependent piezoelectric cantilever

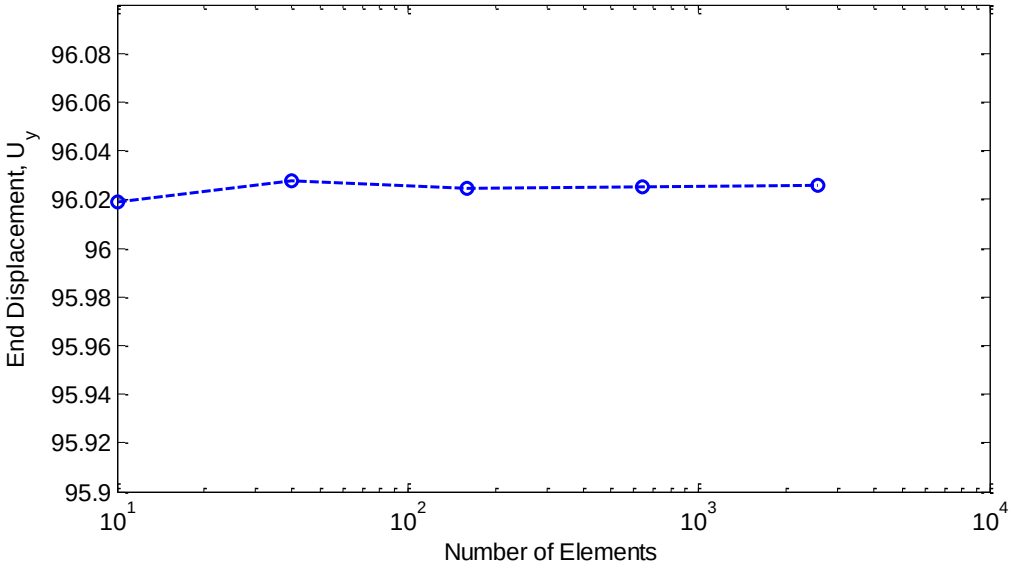

Fig. 17. Convergence of end displacement with mesh refinement

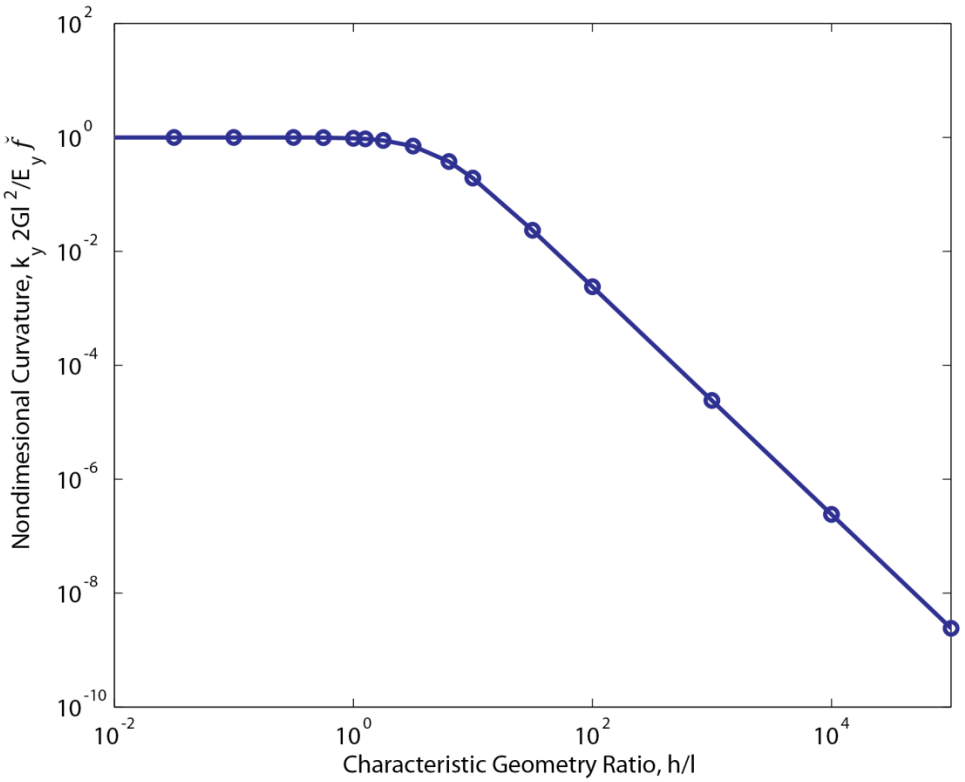

Fig. 18. Nondimensionalized curvature with scaling of cantilever geometry

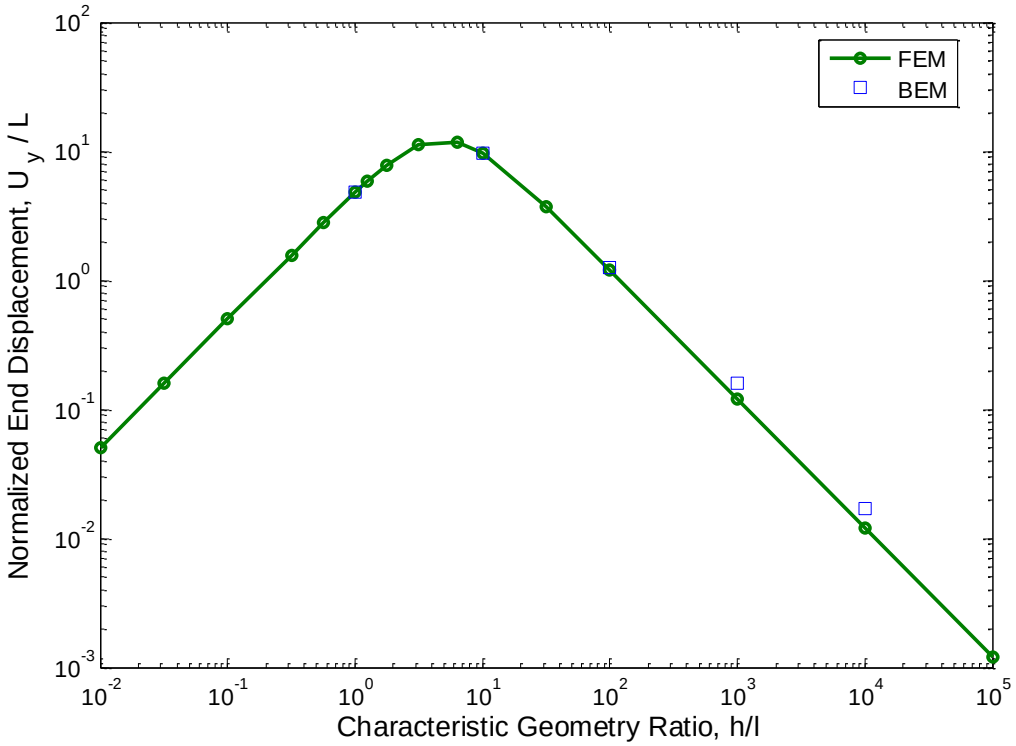

Fig. 19. Ratio of end displacement to length with scaling of cantilever geometry

Finally, we should note that Figs. 18 and 19 include results for $h/l < 1$. With limited experimental data available at this time to estimate the couple-stress parameter size-dependent l, it is not certain that continuum mechanics theories are applicable for length scales in that range. In any case, we believe that it is appropriate to explore the interesting phenomena that size-dependent piezoelectric theory predicts on these minute length scales.

3.4.3 *Slender isotropic cantilever in constant transverse electric field (Barium Titanate ceramic)*

In this section, we analyze a cantilever with the same geometry and boundary conditions as described in the previous section. However, now we consider the material to be Barium Titanate ceramic ($BaTiO_3$) at room temperature, which in single crystal form has cubic centrosymmetric structure. The same mesh from the previous section was used. The beam has characteristic dimension of $h = 1\mu m$ and correspondingly, $L = 20\,\mu m$. The piezoelectric-curvature parameter was approximated based on experiments by Ma and Cross (2006). The other material properties used here were tabulated in Jaffe et al. (1971) and originally measured by Bechmann (1956). As noted above, in single crystal form, this material is centrosymmetric cubic. Based on the measured elastic properties, however, it is clear that the material is not far from being isotropic. As such, for $BaTiO_3$ ceramic, we approximate isotropic elastic coefficients by making the assumption that $G = c_{44},\ \nu = 0.325$ and then use Hooke's law for isotropic materials to calculate an effective Young's modulus. All material properties used here are tabulated in Table 4.

The cantilever was subject to a uniform vertical electric field of $E_y = 1\,V/\mu m$. The vertical end displacement, U_y, was plotted against h/l in Figure 20. Clearly for $BaTiO_3$ the size-dependent piezoelectric effect is not negligible, as an electric field of $1V/\mu m$ causes a vertical end displacement of $U_y \approx 0.4\,\mu m$ (for $h/l > 10$).

Table 4: Approximate $BaTiO_3$ material properties used in simulation

Piezoelectric-curvature parameter, $\check{f}$ $(\mu C/\mu m)$	$\sim 10 \times 10^{-6}$
Young's Modulus, E $(N/\mu m^2)$	113.7×10^{-3}
Shear Modulus, G $(N/\mu m^2)$	42.9×10^{-3}
Permittivity, ε $(\mu C^2/N\mu m^2)$	1.239×10^{-8}

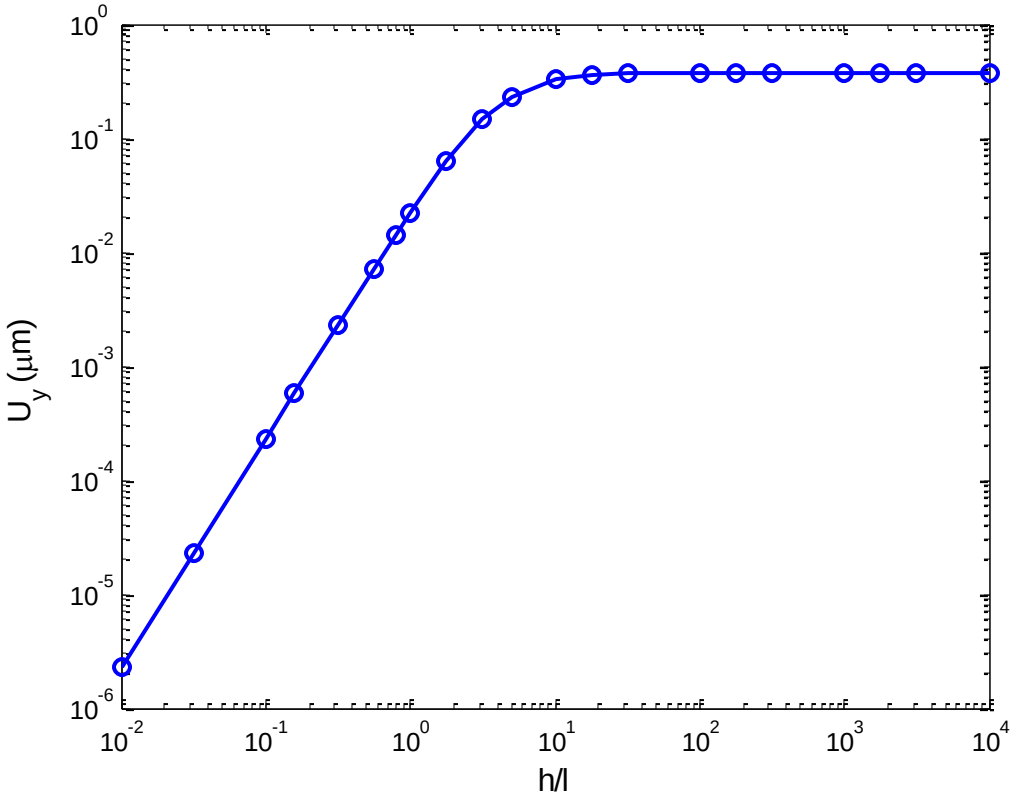

Fig. 20: Vertical end displacement with varying values of l

3.4.4 *Slender isotropic cantilever with transverse end- traction*

This final problem analyzes the induced electric field in an isotropic cantilever subject to end loading under plane-strain conditions. The loading considered here is a transverse shear traction loading with a parabolic distribution. Figure 21 shows a schematic of the problem. The plate has thickness $2a$, where $a = 1/2$ here, and length $L = 20$. For all simulations, we consider the following dimensionless material properties; Young's modulus, $E = 5/2$, Poisson ratio, $\nu = 1/4$, and electric permittivity, $\varepsilon = 1$.

For boundary conditions we consider zero displacement on the left surface as well as zero electric potential at the origin. All surfaces are considered to be electrically insulated, such that $\mathcal{d} = 0$, and also free of moment-tractions. The top and bottom surfaces are tractionless. Finally, the right surface of the plate has an applied shear traction with a parabolic profile, such that $t_y = t_0(1 - y^2/a^2)$.

Figure 22 shows a fill plot of the induced scalar electric potential field. The corresponding field is symmetric and has a maximum value on the bottom surface near the fixed surface at $x = 0$ and a minimum value on the top surface at that same end. Clearly a quantity of interest is the difference between the maximum and minimum value of electric potential. Figure 23 shows a convergence study of the maximum electric potential difference. A coarse mesh with ten rectangular elements was the original mesh. This coarse mesh was systematically refined by dividing each element into four equal

sized rectangular elements. For the purpose of uniformity no localized mesh refinement was considered. Table 5 provides values of the maximum electric potential difference and the maximum end vertical displacement, U_y, for various values of the couple-stress and curvature-piezoelectric parameters for this example of the direct size-dependent piezoelectric effect in an isotropic material

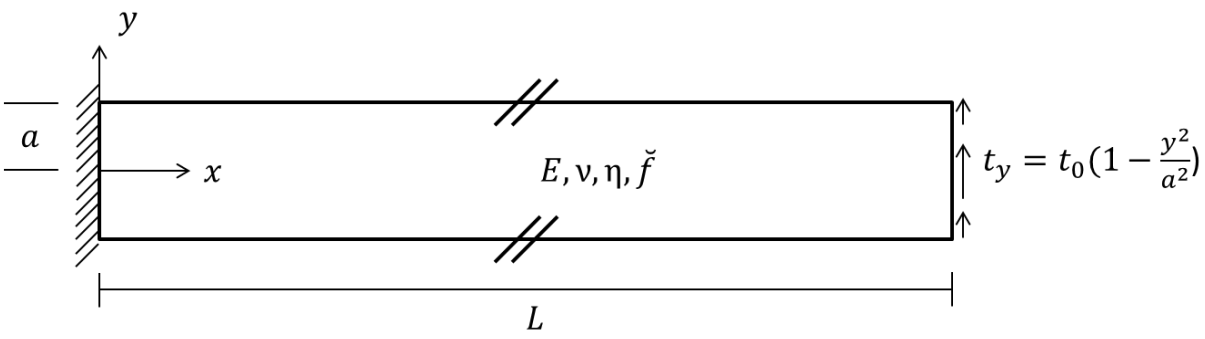

Fig. 21. Problem schematic of long size-dependent piezoelectric cantilever plate

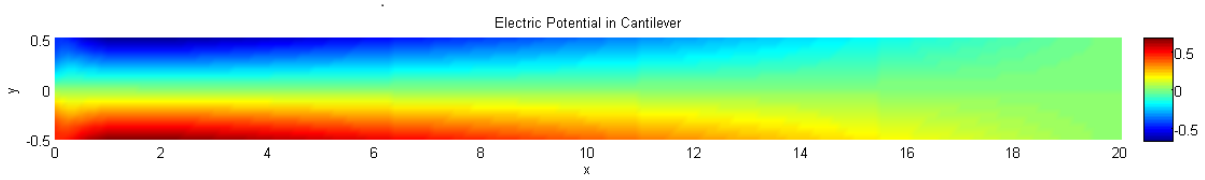

Fig. 22. Plot of electric potential field resulting from transverse loading ($\eta = 1,\ \check{f} = 1$)

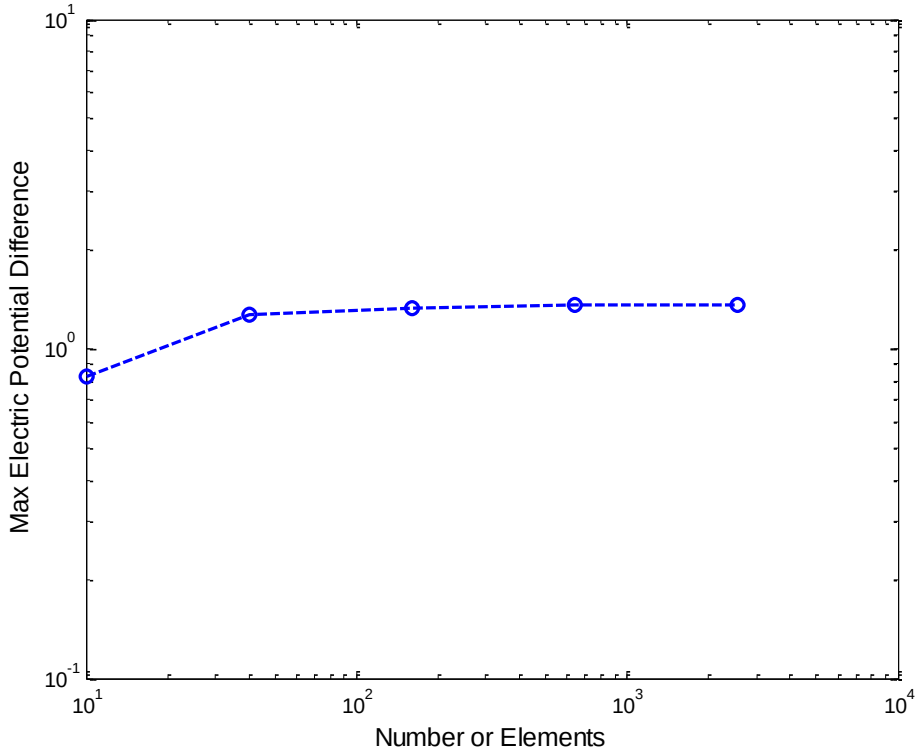

Fig. 23. Convergence of $(\varphi_{max} - \varphi_{min})$ with uniform mesh refinement $(\eta = 1,\ \check{f} = 1)$

Table 5. Results for long size-dependent piezoelectric cantilever plate with transverse end loading, 2560 elements

$\check{f}$	η	$\varphi_{max} - \varphi_{min}$	$U_y \times 10^{-3}$
0.01	0.1	0.9395	7.2061
0.1	0.1	8.8229	6.8181
1	0.1	12.4577	1.6352
1	0.01	13.0643	2.0725
1	1	1.3632	1.6344

CHAPTER FOUR

4.1 Conclusions

Based on the new consistent couple-stress theory for solids (Hadjesfandiari and Dargush, 2011), we have developed a corresponding mixed variational principle and finite element formulation. The formulation presented here considers the rotation field to be separate from the displacement field in the underlying energy statement and then enforces rotation-displacement compatibility via Lagrange multipliers. This is a particularly attractive formulation because the Lagrange multipliers are directly related to the skew-symmetric portion of the stress tensor, which otherwise can be difficult to calculate accurately. Also, the engineering mean curvature vector was defined here and is shown to be the correct energy conjugate deformation vector to the couple-stress vector.

The finite element formulation was then employed to study several problems involving couple-stress phenomena with great accuracy in comparison with both analytical solutions and boundary element analysis. The numerical simulations in section 2.4 showed the size-dependency of couple-stress theory and highlighted three distinct length-scale domains; namely, the classical elasticity domain, the transitional couple-stress domain, and the saturated couple-stress domain. Inclusion of the couple-stress effect was shown to cause potentially large increases in stiffness. Although here we only highlight this transition to shear dominated response for a simple cantilever, this phenomena surely is a more general consequence of the consistent couple stress size-dependent mechanics theory.

The size-dependent piezoelectricity developed in Hadjesfandiari (2013) provides a theory, which couples the electric field and mean curvatures in a manner that is consistent with Maxwell's equations of electromagnetism and skew-symmetric couple stress size-dependent mechanics. Based on this piezoelectric theory, and the mixed variational principle for size-dependent elasticity developed in chapter 2 of the present work, we have developed a mixed finite element formulation for planar couple stress piezoelectric problems in centrosymmetric cubic and isotropic media. This formulation uses Lagrange multipliers to explicitly enforce rotation-displacement compatibility, which reduces the variational problem from having a C^1 to a C^0 continuity requirement. The Lagrange multipliers conveniently are equal to the skew-symmetric portion of the force-stress tensor. However, the resulting system matrix becomes indefinite and care is needed to maintain accuracy in the solver.

The results from the cylinder problem illustrate the convergence characteristics of this formulation compared with an analytical solution for the converse size-dependent piezoelectric effect. Meanwhile, the problem of a cantilever in a uniform transverse electric field showed several interesting results of size-dependent piezoelectricity. For example, it was shown that indeed size-dependent piezoelectric effects are most significant for characteristic geometry on the order of the couple-stress length parameter, l. Also, it was found that at large scales, the size-dependent piezoelectric effects become negligible when compared to the characteristic geometric scale, but do not vanish

completely. It was shown that the size-dependent piezoelectric effect is indeed significant for perovskite ceramics, such as Barium Titanate. The final problem illustrates the direct effect, in which an applied load induces an electric field.

With the exponentially increasing amount of technology that is being developed on the micro and nano-scales the need for tools to analyze size-dependent continuum mechanics problems is greater than ever. Here we have presented simple, robust, and highly accurate finite element formulations based on the consistent couple-stress theory and size-dependent couple stress piezoelectricity. Thus, the current size-dependent couple stress and piezoelectric finite element formulations and their extensions can be expected to provide an excellent tool for doing such analyses and potentially to influence future material, structure and device design over a broad range of applications.

4.2 Future Research

For couple stress elasticity, the extensions to axisymmetric and three dimensional problems are certainly of interest, as is the extension to inelastic response. Perhaps more important though is the need to investigate the predicted effects of couple stress theory through a rigorous program of physical experiments.

For size-dependent piezoelectricity, we have restricted ourselves to consider only centrosymmetric cubic and isotropic materials, where although classical piezoelectric

effects are not present, generally size-dependent piezoelectric effects can occur. Furthermore, while our present finite element formulation is for planar problems, the extensions to axisymmetric and general 3-d problems certainly are of interest. This is especially true in the latter case to enable the comparison with careful physical experiments on cubic single crystals to examine the theory.

References

Allik, H., Hughes, T.J.R., 1970. Finite element method for piezo-electric vibration. Int. J. Num. Meth. Engrg. 2, 151-157.

Amanatidou, E., Aravas, N., 2001. Mixed finite element formulations of strain-gradient elasticity problems. Comp. Meth. App. Mech. Eng. 191, 1723-1751.

Baskaran, S., He, X.T., Chen, Q., Fu, J.Y., 2011. Experimental studies on the direct flexoelectric effect in α-phase polyvinylidene fluoride films. Appl. Phys. Lett. 98, 242901.

Bathe, K.J., 1996. Finite Element Procedures. Prentice Hall, Englewood Cliffs, N.J.

Bechmann, R., 1956. Elastic, piezoelectric, and dielectric constants of polarized barium titanate ceramics and some applicationso of the piezoelectric equations. J. Acoust. Soc. Am. 28, 347-50.

Benjeddou, A., 2000. Advances in piezoelectric finite element modeling of adaptive structural elements: a survey. Comput. Struct. 76, 347-363.

Buhlmann, S., Dwir, B., Baborowski, J., Muralt, P., 2002. Size effects in mesoscopic epitaxial ferroelectric structures: increase of piezoelectric response with decreasing feature-size. Appl. Phys. Lett. 80, 3195-3197.

Cady, W.G., 1964. Piezoelectricity: An Introduction to the Theory and Applications of Electro-mechanical Phenomena in Crystals. Dover, New York.

Catalan, G., Lubk, A., Vlooswijk, A.H.G., Snoeck, E., Magen, C., Janssens, A., Rispens, G., Rijnders, G., Blank, D.H.A., Noheda, B., 2011. Flexoelectric rotation of polarization in ferroelectric thin films. Nat. Mater. 10, 963-967.

Cosserat, E., Cosserat, F., 1909. Théorie des corps déformables (Theory of deformable bodies). A. Hermann et Fils, Paris.

Cross, L.E., 2006. Flexoelectric effects: Charge separation in insulating solids subjected to elastic strain gradients. J. Mater. Sci. 41, 53-63.

Curie, J., Curie, P., 1880. Comptes rendus hebdomadaires des séances de l'Académie des sciences 91, 294-295.

Darrall, B.T., Dargush, G.F., Hadjesfandiari, A.R., 2014. Finite element Lagrange multiplier formulation for size-dependent skew-symmetric couple-stress planar elasticity. Acta Mech. 225, 195-212.

Darrall, B.T., Hadjesfandiari, A.R., Dargush, G.F., 2015. Size-dependent piezoelectricity: A 2D finite element formulation for electric field-mean curvature coupling in dielectrics. Eur. J Mech A-Solid. 49, 308-320.

Davis, T.A., 2004. A column pre-ordering strategy for the unsymmetric-pattern multifrontal method. ACM Trans. Math. Software 30, 165-195.

Davis, T.A., Duff, I.S., 1997. An unsymmetric-pattern multifrontal method for sparse LU factorization. SIAM J. Matrix Anal. Appl. 18, 140-158.

Eliseev, E.A., Morozovska, A.N., Glinchuk, M.D., Blinc, R., 2009. Spontaneous flexoelectric/ flexomagnetic effect in nanoferroics. Phys. Rev. B 79, 165433.

Eringen, A.C., 1968. Theory of micropolar elasticity. In Fracture, Vol. 2, Liebowitz H (ed.). Academic Press, New York, 662–729.

Eringen, A.C., Suhubi, E.S., 1968. Nonlinear theory of simple micro-elastic solids I. Int. J. Eng. Sci. 2, 189-203.

Gaudenzi, P., Bathe, K.J., 1995. An iterative finite-element procedure for the analysis of piezoelectric continua. J. Intell. Mater. Sys. Struct. 6, 266-273.

Griffiths, D.J., 1989. Introduction to Electrodynamics. Prentice Hall, Englewood Cliffs, N.J.

Hadjesfandiari, A.R., 2013. Size-dependent piezoelectricity. Int. J. Solids Struct. 50, 2781-2791.

Hadjesfandiari, A.R., 2014. Size-dependent theories of piezoelectricity: Comparisons and further developments for centrosymmetric dielectrics. Nanotech. In review.

Hadjesfandiari, A.R., 2013. On the skew-symmetric character of the couple-stress tensor. arXiv:1303.3569.

Hadjesfandiari, A.R., Dargush, G.F., 2011. Couple stress theory for solids. Int. J. Solids Struct. 48, 2496-2510.

Hadjesfandiari, A.R., Dargush, G.F., 2013. Fundamental solutions for isotropic size-dependent couple stress elasticity. Int. J. Solids Struct. 50, 1253-1265.

Hadjesfandiari, A.R., Dargush, G.F., 2011. Boundary element formulation for plane problems in couple stress elasticity. Int. J. Numer. Meth. Eng. 89, 618-636.

Harden, J., Mbanga, B., Eber, N., Fodor-Csorba, K., Sprunt, S., Gleeson, J.T., Jakli, A., 2006. Giant flexoelectricity of bent-core nematic liquid crystals. Phys. Rev. Lett. 97, 157802.

Herrmann, L.R., 1983. Mixed finite elements for couple-stress analysis. In Proceedings of the International Symposium on Hybrid and Mixed Finite Element Methods, Atlanta.

Hwang, W.S., Park, H.C., Ha, S.K., 1993. Finite element modeling of piezoelectric sensors and actuators. AIAA J. 31, 930-937.

Jaffe, B., Cook, W. R., Jaffe, H. 1971. Piezoelectric ceramics. Academic Press, New York, N.Y.

Kogan, S.M., 1964. Piezoelectric effect during inhomogeneous deformation and acoustic scattering of carriers in crystals. Sov. Phys. Solid State 5, 2069-2070.

Koiter, W.T., 1964. Couple stresses in the theory of elasticity, I and II. Proc. Kon. Neder. Akad. Weten. B 67, 17-44.

Li, A., Zhou, S., Zhou, S., Wang, B., 2014. Size-dependent analysis of a three-layer microbeam including

electromechanical coupling. Compos. Struct. 116, 120-127.

Ma, W., Cross, L.E. 2006. Flexoelectricity of barium titanate. Appl. Phys. Lett. 88, 232902.

Majdoub, M.S., Sharma, P., Cagin, T., 2008. Enhanced size-dependent piezoelectricity and elasticity in nanostructures due to the flexoelectric effect. Phys. Rev. B 77, 125424.

Maranganti, R., Sharma, P., 2009. Atomistic determination of flexoelectric properties of crystalline dielectrics. Phys. Rev. B 80, 054109.

Maranganti, R., Sharma, N.D., Sharma, P., 2006. Electromechanical coupling in nonpiezoelectric materials due to nanoscale nonlocal size effects: Green's function solutions and embedded inclusions. Phys. Rev. B 74, 014110.

MATLAB (2014). Release 2014a, The MathWorks, Inc., Natick, MA.

Meyer, R.B., 1969. Piezoelectric effects in liquid crystals. Phys. Rev. Lett. 22, 918-921.

Mindlin, R.D., Tiersten, H.F., 1962. Effects of couple-stresses in linear elasticity. Arch. Ration. Mech. Anal. 11, 415-448.

Mindlin, R.D., 1963. Influence of couple-stresses on stress concentration. Exp. Mech. 3, 1-7.

Mindlin, R.D., 1965. Second gradient of strain and surface-tension in linear elasticity. Int. J. Solids Struct. 1, 417-438.

Mindlin, R.D., Eshel, N.N., 1968. On first strain-gradient theories in linear elasticity. Int. J. Solids Struct. 4, 109-124.

Mishima, T., Fujioka, H., Nagakari, S., Kamigaki, K., Nambu, S., 1997. Lattice image observations of nanoscale ordered regions in Pb (Mg1/3Nb2/3)O-3. Jpn. J. App. Phys. 36, 6141-6144.

Nowacki, W., 1986. Theory of Asymmetric Elasticity. Pergamon Press, Oxford.

Padovan, J., 1978. Applications of 3-d finite element procedures to static and dynamic problems in micropolar elasticity. Comput. Struct. 8, 231-236.

Providas, E., Kattis, M.A., 2002. Finite element method for plane Cosserat elasticity. Comput. Struct. 80, 2059-2069.

Resta, R., 2010. Towards a bulk theory of flexoelectricity. Phys. Rev. Lett. 105, 127601.

Sharma, N.D., Maranganti, R., Sharma, P., 2007. On the possibility of piezoelectric nanocomposites without using piezoelectric materials. J. Mech. Phys. Solids 55, 2328-2350.

Shu, J.Y., King, W.E., Fleck, N.A., 1999. Finite elements for materials with strain gradient effects. Int. J. Numer. Meth. in Eng. 44, 373-391.

Shvartsman, V.V., Emelyanov, A.Y., Kholkin, A.L., Safari, A., 2002. Local hysteresis and grain size effects in Pb(Mg1/3Nb2/3)O-SbTiO3. Appl. Phys. Lett. 81, 117-119.

Tagantsev, A.K., 1986. Piezoelectricity and flexoelectricity in crystalline dielectrics. Phys. Rev. B 34, 5883-5889.

Toupin, R.A., 1962. Elastic materials with couple-stresses. Arch. Ration. Mech. Anal. 11, 385-414.

Voigt W., 1887. Theoretische Studien über die Elastizitätsverhältnisse der Kristalle (Theoretical studies on the elasticity relationships of crystals). Abhandlungen der Gesellschaft der Wissenschaften zu Göttingen. 34.

Voigt, W., 1910. Lehrbuch der Kristallphysik. BG Teubner, Berlin.

Wang, G.F., Yu, S.W., Feng, X.Q., 2004. A piezoelectric constitutive theory with rotation gradient effects. Eur. J. Mech. A/Solids 23, 455-466.

Wood, R.D., 1988. Finite element analysis of plane couple-stress problems using first order stress functions. Int. J. Numer. Meth. Eng. 26, 489-509.

Yudin, P.V., Tagantsev, A.K., 2013. Fundamentals of flexoelectricity in solids. Nanotechnology 24, 432001.

Zhu, W., Fu, J.Y., Li, N., Cross, L.E., 2006. Piezoelectric composite based on the enhanced flexoelectric effects. Appl. Phys. Lett. 89, 192904.

Zienkiewicz, O.C., Taylor, R.L., 2000. The Finite Element Method. Butterworth-Heinemann, Oxford.

Zubko, P., Catalan, G., Buckley, A., Welche, P.R.L., Scott, J.F., 2007. Strain-gradient-induced polarization in SrTiO3 single crystals. Phys. Rev. Lett. 99, 167601.

Zubko, P., Catalan, G., Tagantsev, A.K., 2013. Flexoelectric effect in solids. Ann. Rev. Mater. Res. 43, 387-421.